A Near Glimpse into a Distant Past: Chemical Analyses of Ancient Milky Way Satellite Galaxies using High-Resolution Stellar Spectroscopy

by

D. F. Waller
B.Sc., University of Victoria, 2020

A Thesis Submitted in Partial Fulfillment of the
Requirements for the Degree of

MASTER OF SCIENCE

in the Department of Physics and Astronomy

A Near Glimpse into a Distant Past: Chemical Analyses of Ancient Milky Way Satellite Galaxies using High-Resolution Stellar Spectroscopy

by

D. F. Waller
B.Sc., University of Victoria, 2020

Supervisory Committee

Dr. K. Venn, Co-Supervisor
(Physics and Astronomy)

Dr. A. McConnachie, Co-Supervisor
(Physics and Astronomy)

Abstract

The least-luminous galaxies ever detected, ultra-faint dwarf (UFD) galaxies, are ancient, metal-poor, dark-matter dominated, and likely represent the floor of the galaxy luminosity function. Their stars preserve the signatures from early chemical evolution, and their dark matter haloes are testing grounds for ΛCDM cosmological models.

UFDs are subject to tidal interactions with the Milky Way and dwarfs, which visually range from disrupted streams to slightly elongated structures. An extended structure may also be the result of a minor merger of dwarfs. To further our understanding of these extended structures, we examine high-resolution spectra of stars in the outskirts of UFDs. It is expected that signatures of one or just a few early supernovae may be detectable in the chemical abundance patterns of UFD stars. High-resolution spectroscopy of the brightest individual stars allows us to recover these signatures, and piece together the chemodynamical history of these galaxies. We use Gemini/GRACES to obtain high-resolution spectra of potential members in the outskirts of three ultra-faint dwarf (UFD) galaxies: Coma Berenices ($>2R_h$), Ursa Major I ($4R_h$), and Boötes I ($4R_h$), as well as a new member in the central region of Ursa Major I (where the half-light radius R_h is the radius within which half of the galaxy's light is contained, measured along the semi-major axis). Targets were selected with a new Bayesian technique which uses Gaia EDR3 photometry and astrometry to determine stellar membership to UFDs. All 5 stars are determined to be members by precision radial velocities and metallicities that confirm their associations with the UFD galaxies. The spectra were also used to measure absorption lines for 10 elements (Na, Mg, K, Ca, Sc, Ti, Cr, Fe, Ni, and Ba), which confirm that the chemical abundances of the outermost stars are in good agreement with stars in the central regions. The abundance ratios and chemical patterns of the stars in Coma Berenices are consistent with contributions from SN Ia, which is unusual for its star formation history and in conflict with previous suggestions that this system evolved chemically from a single core collapse supernova event. The chemistries for all three galaxies are consistent with the outermost stars forming in the central regions, then moving to their current locations through tidal stripping and/or supernova feedback. In Boötes I, however, the lower metallicity and lack of strong carbon enrichment of its outermost stars could also be evidence of a dwarf galaxy merger.

To pursue further high-resolution spectroscopic observations of UFD stars, I carried out an internship at the Gemini South telescope Observatory which was timed

with the commissioning of the Gemini High Resolution Optical SpecTrograph (GHOST). Target selection, logkeeping, early data reduction, calibration tests and instrument operation tasks were completed during 17 nights of commissioning between June and September 2022.

Since commissioning, I performed bug-testing and developed streamlined methods for processing data to work towards completion and refinement of the data reduction pipeline. With this experience and relative expertise, I worked with the science team towards the goal of publishing our first science results. GHOST has been integrated into the Gemini instrumentation suite and is available for observing proposals.

Contents

List of Tables

List of Figures

Acknowledgements

This thesis was conducted primarily at the University of Victoria, which stands on the traditional, unceded territory of the lək$^{\text{w}}$ə$\dot{\text{ŋ}}$ən peoples. I would like to acknowledge with respect the Songhees, Esquimalt, and W̱SÁNEĆ peoples, on whose land I have found my home. Their continued stewardship is crucial to preservation of this land.

I would like to thank:

Emmett, Gabe, and Jane without whom I would not have made it through the writing, the living abroad, and the research. Thank you for board game nights and mornings, for meals and snacks, for sharing queer media, for the many swims, and for your uncomplicated, trusting, gentle love.

Kim Venn, for believing in me when I did not in myself, and for going above and beyond as a mentor to help me see this through.

the GHOST teams at Gemini, UVic, NRC, and ANU, for creating a beautiful spectrograph, teaching me all about it, and accepting the help I could give.

the graduate students and post-docs in my group and cohort, for your compassion, your camaraderie, your commiseration and your community. I am so excited to see where you take your futures.

Cindy Kutyn, a benevolent spirit often spotted in the admin office wielding kindness in the form of sticker sheets. Thank you for saying hi every morning.

Vladimir Catimir, for never doing anything wrong in your life.

Annora, a friend who gave. Look, I finished! I can finally tell you that I'll be staying a while. Thank you for showing me how beautiful life is here on earth.

every friend and houseguest, for brunches, lunches, potlucks and parties. You are the reason I continue.

my family, for giving me one of the greatest gifts: time.

Not all exits are made equal. Some are beautiful, and poetic, and satisfying. Others are abrupt and unfair. But most are unremarkable, unintentional, clumsy.
Griffin McElroy

Dedication

to the theys, gays, and strays making their own way on this blue marble.
May you call it home for as long as your atoms allow,
and may the rest of us know you as home, for as long as your actions echo.

Chapter 1

Introduction

1.1 On Understanding Our Origins

We study old things and past events to better understand the present and future. A geologist may examine old rocks, a historian old documents, an economist old market trends. The nature of inquiry will change from field to field, but the practice of understanding the 'before' in order to understand the 'now' and the 'later' is common. Light pouring down from the heavens is a historical record, and physics is the cipher, allowing the record to be decoded. In this thesis, I present an investigation on the chemical and evolutionary history of ancient, nearby galaxies, providing insight into the conditions of the very early universe; this is my contribution to a better understanding of a question as old as humanity itself: how did it all begin?.

The night sky provides access to a collection of the oldest things to ever exist. The Hubble and JWST telescopes have seen galaxies as they were in the first 500 Myr of the universe (Oesch et al., 2014; Curtis-Lake et al., 2023), challenging our understanding of galaxy formation (Heintz et al., 2023). However, these observations are by nature of extremely distant objects. If so much can be learned by observing very old and distant things, then we must also attempt to investigate the very old and nearby.

Some of the stars which formed in the gas clouds of the early universe are still present in the Milky Way today, and they preserve the chemical properties from that time in their atmospheres. While age can be difficult to determine for a single star, it is much easier to estimate age for a population of stars. Remnants of old stellar populations such as Gaia-Sausage-Enceladus (GSE) galaxy (Belokurov et al., 2018; Helmi et al., 2018) or globular clusters such as the extremely metal-poor C-19 (Martin et al., 2022b) were discovered as stellar streams in the halo, stretched around

the Milky Way by merger events. These discoveries are consistent with the current understanding of hierarchical galaxy formation: smaller structures come together to make larger ones (White & Rees, 1978; Frenk et al., 1988). Just outside the galaxy in the Local Group dwarf galaxies orbit the Milky Way just as GSE and C-19 once did. Studying the old stellar populations of these satellite dwarf galaxies is an important component in understanding the early universe.

1.2 Introducing UFDs

Amongst the Milky Way satellites exist the least-luminous galaxies ever detected, called Ultra-Faint Dwarf galaxies (UFDs) (Simon, 2019). They are thought to be surviving relics of the first galaxies, and their stars preserve the signatures from early chemical evolution in the universe. I will summarize the trail of inquisition that has lead to these conclusions, and discuss some of the ways they are studied.

The study of UFDs is quite young, coming into being entirely within the past couple of decades. As can be seen in Figure 1.1, the advent of digital surveys like the SDSS, DES and Pan-STARRS made possible new discoveries of extremely low surface-brightness groups of stars. Within 15 years, the known population of Milky Way satellite galaxies had increased from ∼10 to nearly 60. This represents a dramatic expansion in our knowledge of the galactic neighborhood, and kick-started a new way to study the ancient universe.

Dwarf galaxies known prior to 2005 have absolute magnitudes brighter than M_V=−8.7. These new systems are much fainter, and Simon (2019) suggests that any galaxies with absolute magnitudes fainter than M_V=−7.7 be considered UFDs. Because of their distances (10s-100s kpc), only the brightest stars in UFD galaxies could be initially detected. Often, mere dozens of bright stars were the signpost that a UFD existed at all (Smith et al., 2023). Despite being often compared to globular clusters (GCs), UFDs have many distinct characteristics, one of which is their physical extents. One of the largest GCs, Ω Cen, has a mass on the order of $\sim 10^6 M_\odot$and a half-light radius[1] of only r_h ∼6pc (van de Ven et al., 2006), while a fairly small UFD Coma Berenices has a similar mass ($\sim 10^6 M_\odot$) with a much larger half-light radius of r_h = 65pc (McConnachie, 2012). GCs are dense and dynamically

[1] where R_h is the radius within which half of the galaxy's light is contained, measured along the semi-major axis.

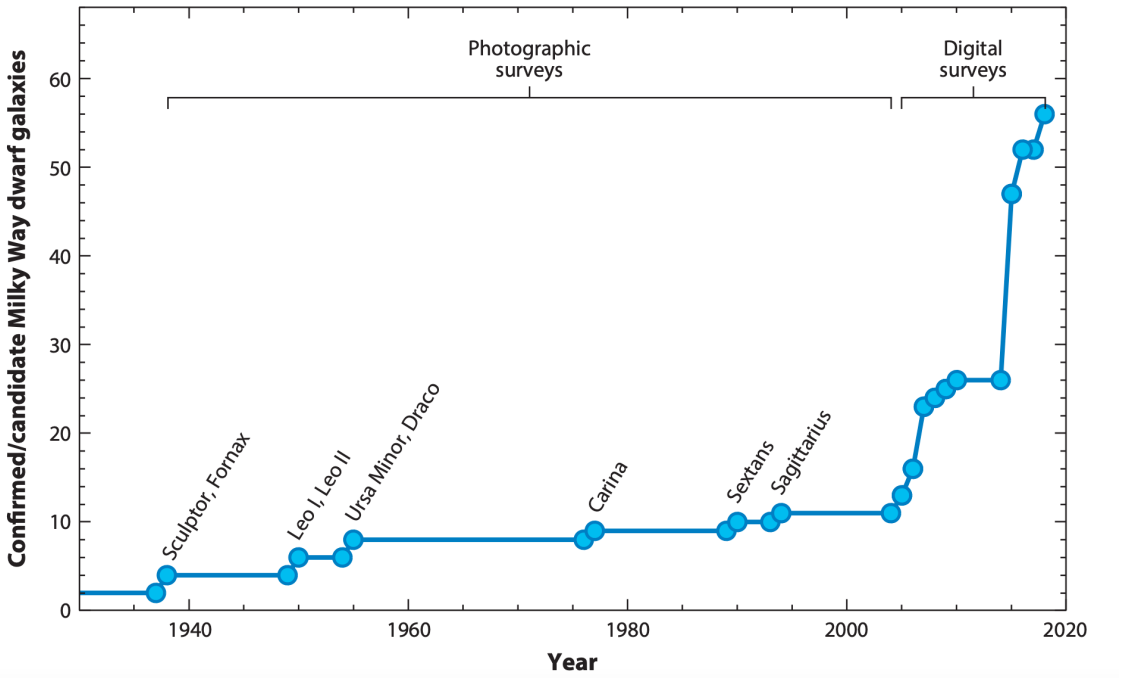

Figure 1.1: Census of Milky Way satellite galaxies as a function of time. The objects shown here include all spectroscopically confirmed dwarf galaxies as well as those suspected to be dwarfs based on less conclusive spectroscopic and photometric measurements. The major discovery impact of the Sloan Digital Sky Survey (SDSS, York et al. (2000); Abazajian et al. (2009)), the Dark Energy Survey (DES, Abbott et al. (2018)), and the Panoramic Survey Telescope & Rapid Response System (Pan-STARRS, Chambers et al. (2016)), each of which approximately doubled the previously known satellite population, stands out in this historical perspective. Source: Simon (2019)

relaxed with velocity dispersions that imply mass-to-light (M/L) ratios ~ 1[2] (Baumgardt & Hilker, 2018), while UFDs are fluffy and loose conglomerations of stars with velocity dispersions that indicate M/L ratios in the hundreds (Simon & Geha, 2007). This demonstrates that UFDs cannot be purely baryonic systems, and must be very dark-matter dominated.

The mean stellar metallicities[3] of UFDs are also often quite low (McConnachie, 2012). Metallicity is negatively associated with age because the first stars and sub-

[2]The sun has a M/L=1, so a GC with M/L$\sim$1 must have most of its matter in the forms of baryons in stars.

[3]Metallicity is a measure of metals (non- hydrogen or helium elements), but often iron abundance is used a surrogate for total metallicity, notated as Fe/H. It is scaled to solar values using standard notation $[X/Y] = \log n(X)/n(Y)_* - \log n(X)/n(Y)_\odot$, where n(X) and n(Y) are column densities (in cm^{-2}) such that [Fe/H] = 0 is solar value, -1 is 10 times less, -2 is 100 times less, etc.

sequent stellar generations synthesize the cosmic primordial gas of mostly H, He and Li into heavier elements such as C, O, Ne, Mg, Si, Fe and beyond, gradually increasing the ratios of metals to hydrogen. Therefore, low metallicities in UFDs imply their stars are very old and formed in the early universe. UFDs possess the smallest dark-matter haloes known (Simon, 2019), and simulations show that halo masses any smaller would have insufficient gravity to hold onto its baryons against the ionizing radiation pressure from the first massive stars (Ricotti et al., 2008). These shallow potential wells make them sensitive to environmental conditions, which makes them good tests of the interplay between stellar feedback and gas retention in ΛCDM cosmology (Bullock & Boylan-Kolchin, 2017a), the evolution of faint galaxies in the Milky Way environment (Wheeler et al., 2015; Akins et al., 2021), and the quenching effects of reionization (Wetzel et al., 2015; Rey et al., 2020). In addition, recent hydrodynamical simulations of low mass galaxies embedded in dark matter halos have shown that star formation is quenched at very early times, consistent with quenching from cosmic reionization (Wheeler et al., 2019; Applebaum et al., 2021). This is similar to the star-forming histories for some UFDs reconstructed from HST and Keck/DEIMOS data (Brown et al., 2014; Bechtol et al., 2015), suggesting that UFDs have remained unchanged since the first 1-2 billion years of the universe, and are possibly the modern day relics of the earliest galaxies.

While UFDs can be identified by spotting over-densities of stars, determining which stars are members and which are background or foreground stars can be challenging. This is often done by combining a star's physical location, 2D on-sky velocity, line-of-sight velocity, metallicity, brightness, and colour variety of measurements and assigning probabilities to each star based on the fit to the whole system (McConnachie & Venn, 2020a; Battaglia et al., 2022; Pace et al., 2022). A centrally located star with a radial velocity significantly outside the distribution can be safely ruled out, however, a distantly placed star that matches all other properties cannot. Just as the Milky Way has very distant stars in the halo, UFDs may have similar extended structures (Deason et al., 2022). For a UFD such as Coma Berenices, many known member stars are located within $r_h \sim 1$ (Simon & Geha, 2007) with very few beyond that . An algorithm which does not take physical location into account may be capable of finding stars in such extended structures. Such stars may have chemical differences, giving insight to possible merger histories of UFDs (Chiti et al., 2021; Roederer et al., 2023; Sestito et al., 2023). Chapter 3 presents an analysis of 5 UFD member stars, 4 of which are beyond $2r_h$, all of which were discovered using the algorithm described

in McConnachie & Venn (2020a); Jensen et al. (2024).

Studying UFDs requires a variety of astrometric, photometric and spectroscopic techniques. The ESO space telescope Gaia (Gaia Collaboration et al., 2016a) jump-started a revolution in the study of local stellar structures like streams, GCs, dSphs and UFDs (Helmi, 2020). Gaia astrometrically tracks year after year the positions and parallaxes of 1.3 billion sources down to magnitude G $\sim$ 21, and detects radial velocities from low-resolution spectra (R=11500 (Cropper et al., 2018)) for 7.2 million stars brighter than G = 12 (Gaia Collaboration et al., 2018b). This means that full 3D positions and velocities are tracked for all 7.2 million of those stars.

Gaia provides photometric magnitudes with 3 filters, BP, RP, and G. These are combined to make Gaia colour-magnitude diagrams (CMD) in G vs (BP-RP), which are shown in Chapter 3.1. CMDs reveal patterns that trace out the evolutionary paths of stars. Models of evolutionary tracks called isochrones can be used to estimate age, temperature, gravity, and distances to stars (VandenBerg et al., 2000).

While the work presented in this thesis makes abundant use of photometric and astrometric resources, my work will focus on the use of high-resolution (R>50 000) spectroscopic methods to investigate the nature of UFDs.

1.3 High Resolution Spectroscopy for the Study of UFDs

1.3.1 How is Spectroscopy useful?

Spectroscopy is the study of light and its interactions with matter, done by separating light into its component wavelengths[4]. Spectroscopy can be done in any wavelength of light, from long radio waves to short x-rays, but this thesis will focus on "visible light", the wavelengths of light which human eyes are good at detecting. Many individual's first experiences with a spectrum is a rainbow—light from the sun refracted within water droplets. In order to gather stellar spectra from stars much farther away than the sun, astronomers use reflective gratings rather than water droplets.

An enormous wealth of information is stored in the spectrum of a star. Cores of stars produce photons in a smooth continuum known as a blackbody, but sections of that continuum are altered when the photons interact with, or are absorbed by matter. Matter is very picky in its energy diet, so it can only interact with specific wavelengths of light. This can be seen in Figure 1.2, where thin dark bands in the sun's

[4]or frequencies or energies, depending on the field. For the visible spectrum of light, wavelength in units of Angstroms ($\mathring{A}$) is conventional.

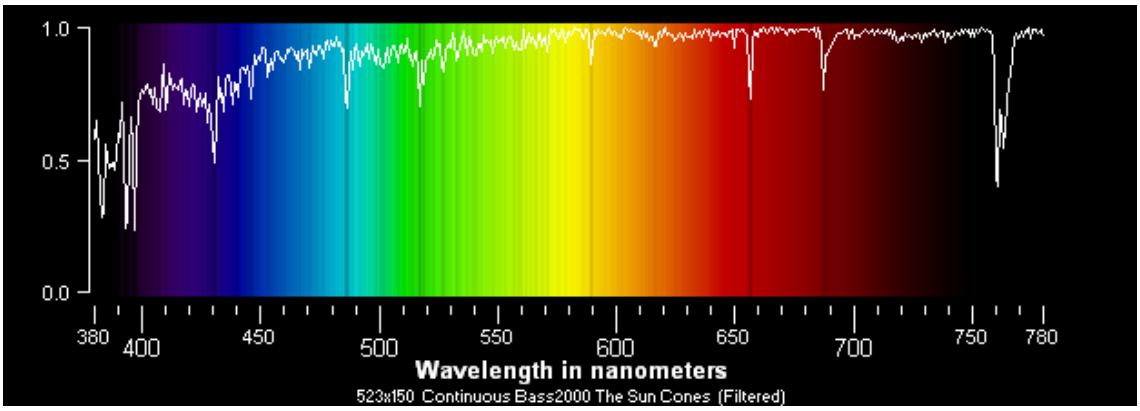

Figure 1.2: A solar spectrum in the visible waveband. White lines show the normalized intensity of light at a given wavelength, the colours show the corresponding colour for wavelengths, and the dark lines are absorption lines caused by matter in the sun's and earth's atmospheres removing light of that wavelength, Source: McNish (2018).

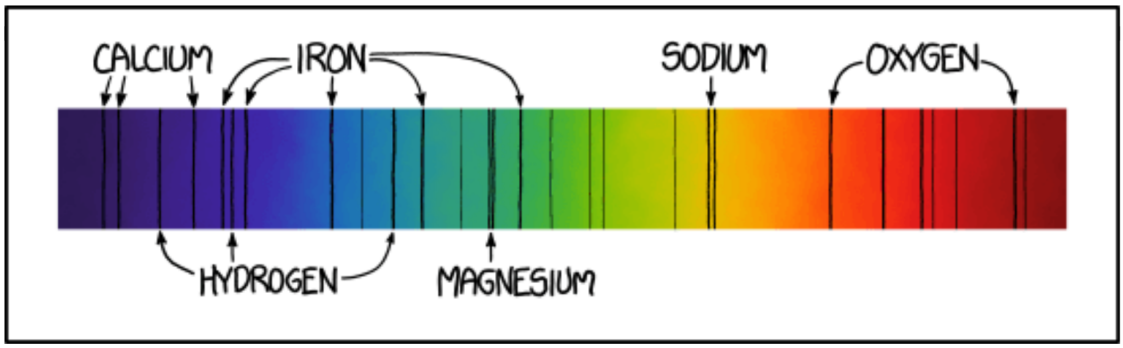

Figure 1.3: A cartoon of prominent absorption lines in the solar spectrum. Source: Munroe (2016).

rainbow continuum correspond to dips in intensity shown in the white line. Different elements (e.g. carbon, iron), possessing different chemical properties, will interact differently, creating a unique pattern often compared to a human's fingerprint. By studying elements here on earth, precise knowledge of what the 'fingerprint' of each element looks like can be compared to spectral lines seen in stars. Figure 1.3 shows a cartoon of some spectral lines in the sun and the elements responsible for creating them.

The light generated in the centers of stars needs to pass through the cooler stellar atmosphere, where all the present elements will absorb their signature wavelengths of light. It is through this mechanism that one can determine what concentration of an element exists within the atmospheres of very distant stars. A larger amount of one

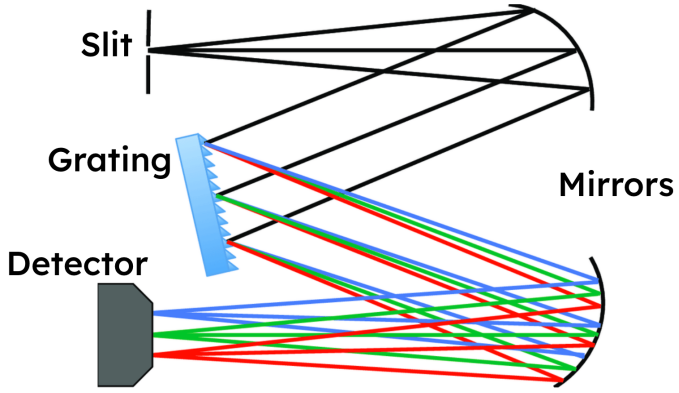

Figure 1.4: A basic single-grating spectrograph design. Light passed through the slit is separated by the grating and focused on to a CCD detector. Source: Burgers (2015).

element will cause a deeper, darker absorption line.

Another use for spectroscopy is measuring radial velocity. This can be done by measuring the 'redshift', the light-equivalent of the Doppler Effect in sound waves. Radial velocity is necessary to know the 3D motion of an object, which allows us study the dynamics of a system, and is a component for determining stellar memberships of UFDs.

1.3.2 Basic Spectrograph Design

Spectrographs are instruments which turn light from a telescope into a spectrum. Modern spectrographs are complicated arrays of slits, mirrors, gratings, and cameras, but a basic design consists of a slit, disperser, detector, and some reflective or refractive optical components. A visual example is given in Figure 1.4.

The slit allows only a narrow strip of light to pass through. A wide slit will result in overlapping images of different wavelengths in the final result, smearing the spectrum and reducing the resolution in the spectrum. However, a narrow slit will allow less light to pass through, meaning that more time may be needed to collect enough light. This trade-off can be avoided by designing a 'pseudo-slit' with the use of fibre-optic cables. Light from a star is sent into a small bundle of fibers, which are then re-arranged to output the light in a line similar to a slit. This allows for both resolution and throughput to be maximized.

The disperser separates the light into component wavelengths. Historically, and in popular culture, this element would be a prism. Common practice in astronomy now

is to use a reflective grating, a surface with grooves so fine that different wavelengths of light reflect at different angles[5]. A grating disperses a spectrum into a rectangle shape with red light at one end and blue light at the other. In order to increase the resolution of this spectrum, the rectangle must get longer, with red getting farther away from blue. Because CCD detectors are square and limited in size, this is an impractical way to increase the resolution of the spectrum. In order to maximise resolution, some spectrographs will include a cross-dispersing element. A cross-disperser works by dispersing the light in two directions, creating stacked rows of spectra called 'orders', as can be seen in Figure 1.5. This arrangement, called an echelle spectrograph, packs much more spectral resolution onto one square detector chip, but it comes with trade-offs and added complexities.

1.3.3 Spectrograph considerations for the study of UFDs

The high-resolution capabilities of echelle spectrographs is necessary for measuring stellar chemical abundances. In the bottom half of Figure 1.5, a myriad of spectral lines can be seen. There are only a few lines which are strong enough to be measured using low-res or even narrow-bandpass photometry (eg. Ca H&K, seen as wide dark patches in the bottom quarter of Figure 1.5); most spectral lines are quite small in comparison. The trade-off one makes for a high-resolution, however, is less flux per unit wavelength. Light is spread out over a larger area, so more observing time will be needed to achieve a sufficient signal-to-noise ratio per pixel. This makes high-resolution observations quite time-costly; many hours a night may be dedicated to a single object. The targets of such an investment must be selected carefully in order to maximise telescope resources.

Chapter 2 of this thesis will focus on the newly-commissioned Gemini High Resolution Optical SpecTrograph (GHOST) at the Gemini South Telescope (McConnachie et al., 2024). This spectrograph is well-suited for taking observations from which detailed chemical abundances of stars in UFDs may be measured (Hayes et al., 2023).

1.4 Chemodynamical analyses of UFDs

The oldest stars preserve the signatures from the earliest stages of chemical evolution in a galaxy. It is expected that signatures of one or just a few early supernovae may

[5]This is the same principle that causes a bird feather or the back of a CD to reflect light in rainbow hues.

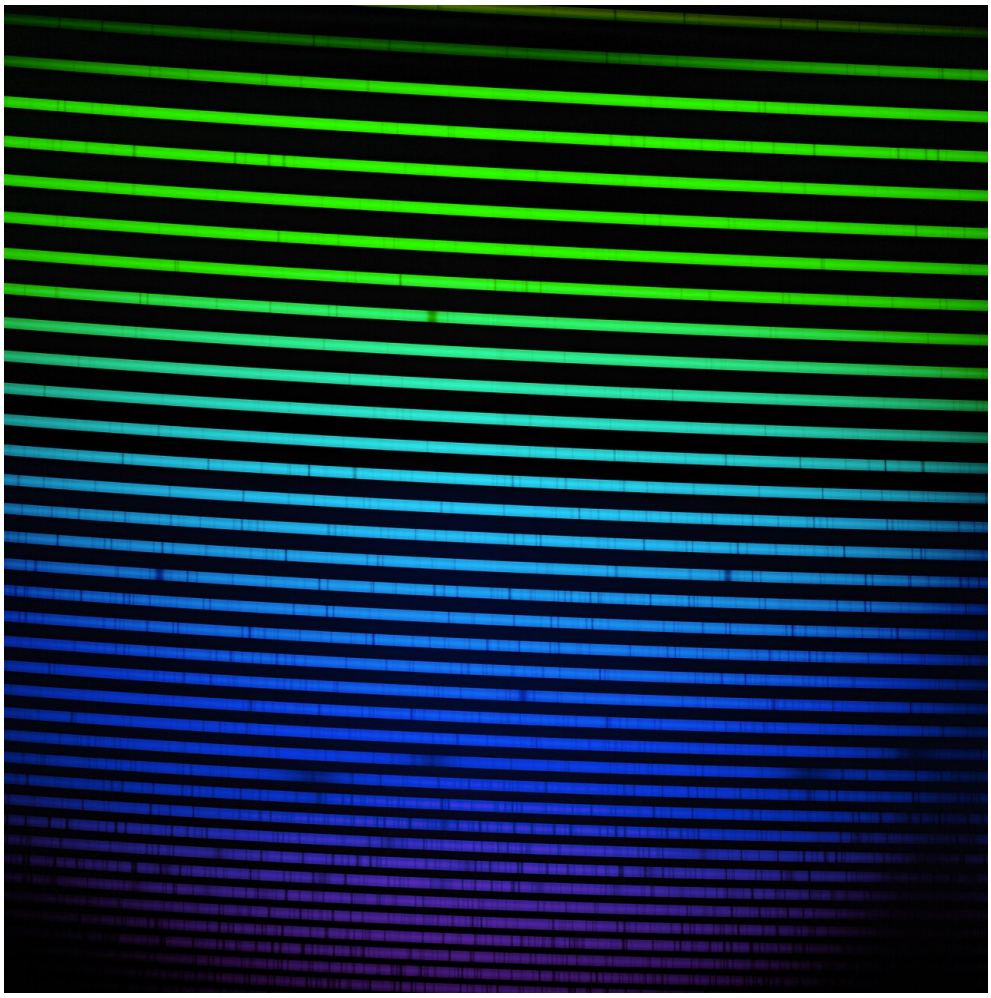

Figure 1.5: The GHOST blue-arm spectrum of HD 222925 shows the striping orders of an echelle spectrograph, and demonstrates the fine spectral detail obtainable with such an instrument. The colours are a close approximation of the true colours the human eye would see. Source: NOIRLab et al. (2022).

be detectable in the chemical abundance patterns of stars in the very low mass and ancient UFD galaxies. High-resolution spectroscopy of the brightest individual stars allows us to recover these signatures, and piece together the chemodynamical histories of the individual UFD galaxies.

1.4.1 Chemical Categories

When considering the chemical compositions of stars, it is useful to categorize elements by their formation mechanism. All metals are produced through some nucleosynthetic pathway, such as fusion in the cores of stars or in high-energy events like

supernovae or compact binary mergers. Either way, some mechanism is necessary to transport metals from the core of a star into the interstellar medium so they can be part of a new generation of star-formation (Kobayashi et al., 2020b). The nucleosynthesis groups that will be discussed are alpha-capture, odd-Z (Z in this case indicates the atomic number of an element), iron-peak, and neutron-capture.

1.4.1.a Alpha Elements

Alpha elements are even-Z elements (eg. Mg, Ca, Si, Ti) which form primarily from helium nuclei captures during the carbon-, neon- and silicon-burning phases of massive star evolution (Timmes et al., 1995; Kobayashi et al., 2006), and through the α-rich freeze-out during core collapse supernovae (Woosley & Hoffman, 1992). This results in an over-abundance of elements with even atomic numbers, and an under-abundance of odd atomic numbers, a phenomenon known as the odd-even effect (Heger & Woosley, 2010; Takahashi et al., 2018). Alpha elements reach the interstellar medium via core-collapse supernova, so they can be treated like a kind of clock, measuring successive generations of massive stars. This will be discussed further in section 1.4.1.b

1.4.1.b Iron-Peak Elements

Iron-peak elements like iron, chromium and nickel (Fe, Cr, Ni) are formed primarily in two events, (i) SNII: the core-collapse supernova of a massive star (Woosley & Weaver, 1995; Heger & Woosley, 2010; Kobayashi et al., 2020b) and (ii) SNIa: a white dwarf in a single or double degenerate binary system going supernova after reaching critical mass (Kobayashi & Nomoto, 2009; Nomoto et al., 2013). The white dwarfs in SNIa are the remnants of low-mass stars ($<8M_{\odot}$, Kobayashi et al. (2020a)), which take longer to evolve than the high-mass stars ($>8M_{\odot}$) that end their lives in a Type II supernova. This results in a delay-time between SNII and SNIa enrichment of the ISM. For very old populations of stars, both iron-peak and alpha elements will present in roughly constant proportions because it is all from the same core-collapse supernova source. Once enough time has elapsed that SNIa are contributing, iron increases dramatically in proportion to alpha elements. This results in an "Alpha-knee" when examining the evolution of the [alpha/Fe] abundances with increasing [Fe/H] in a galaxy (Vincenzo et al., 2018), and can be seen in Figure 1.6 where the older thick disk of the Milky Way has a higher α/Fe ratio than the younger thin disk (Imig et al., 2023).

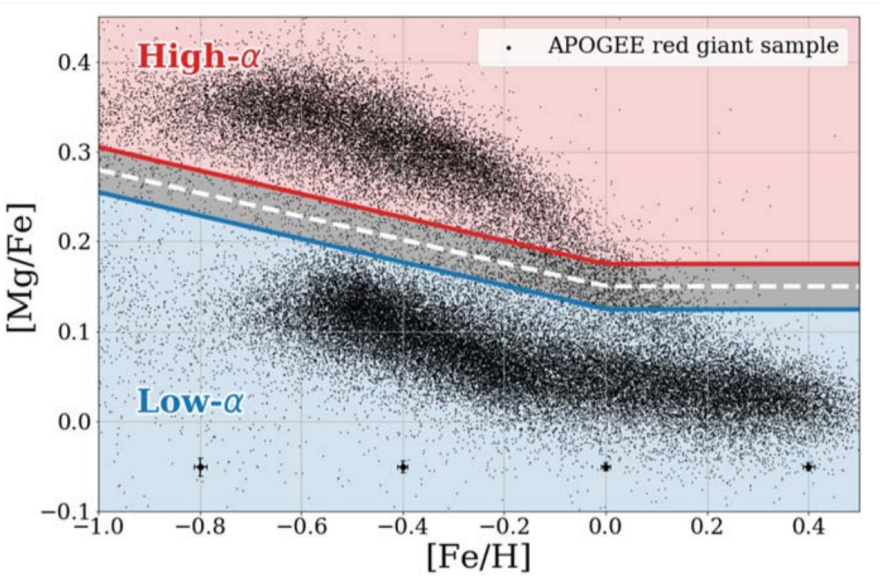

Figure 1.6: The [Mg/Fe]–[Fe/H] plane for red giant stars (black points) in the APOGEE sample, demonstrating the low-α (blue) of the thin disk and high-α (red) of the thick disk. The gray region is an added buffer zone due to abundance uncertainties. Source: Imig et al. (2023)

1.4.1.c Neutron-capture Elements

Neutron-capture elements form by atomic nuclei capturing free neutrons which radioactively decay to protons. If the neutron flux is high enough that multiple neutrons are captured before decay can happen, it is called rapid neutron capture (r-process), but if the neutron flux is low such that decay can happen before another neutron capture, it is called slow (s-process) (Seeger et al., 1965). High neutron fluxes occur primarily in neutron stars mergers (NSM) (Tanvir et al., 2017a), but also in small amounts during CCSN from photo-dissociation of iron (Wanajo, 2013). The primary s-process environment is during thermal pulsing in asymptotic giant branch (AGB) stars (Busso et al., 1999). Enrichment from NSM and AGB stars has a longer delay-time than enrichment from CCSN, so [s/Fe] or [r/Fe][6] ratios can be used to track chemical evolution (Skúladóttir et al., 2019).

Barium (Ba) is produced by both by s- and r-process (Skúladóttir et al., 2019), and it has a few lines strong enough and in the right wavelength range (5000-7000$\AA$) to be detected by most HR spectrographs. It is expected that some stars may have

[6]where [X/Fe] = $\log(\mathrm{X/Fe})_* - \log(\mathrm{X/Fe})_\odot$ and s and r are a stand-in for elements produced by s- and r-process.

a very low [Ba/Fe] abundance which represents the floor of r-process enrichment from CCSN, without any contributions from NSM or AGB (Frebel & Bromm, 2012). Europium (Eu) is almost strictly created through the r-process (Bisterzo et al., 2014), which makes it a good tracer for NSM. It has only one weak line within the typical wavelength ranges of the Gemini/GRACES spectrograph at 6645$\mathring{A}$, so a very high SNR is required to measure it. However, stronger lines exist in the bluer end of the spectrum ($\sim$4000$\mathring{A}$), so HR spectrographs with good response in the blue (e.g. GHOST, dicussed in section 2.1) are imperative for observing interesting neutron-capture ratios in UFDs.

Most UFDs do not show strong r-process signatures characteristic of NSMs because these are rare events which are statistically unlikely to happen with such small populations of stars. An exception being Reticulum II, which has many stars with a very enhanced r-process signature, and a few stars with none (Ji et al., 2016; Roederer et al., 2016; Hayes et al., 2023). This suggests that part of the ISM of Reticulum II was enriched by just one NSM before it quenched (Ji et al., 2023). Some UFD stars show very low upper limits to their [Ba/Fe] (Frebel et al., 2010b), suggesting UFDs undergo stochastic star-formation.

1.4.1.d Odd-z Elements

Odd-Z elements such as sodium, potassium, and scandium (Na, K, and Sc) form through neutron-capture at low atomic numbers, and are important indicators of core collapse supernova yields, as the lower energetic requirements for α particle capture versus higher for neutron capture produces a noticeable odd-even effect in the predicted yields (Heger & Woosley, 2010; Takahashi et al., 2018). Thusly, a strong odd-even effect in very metal-poor stars is taken as evidence of enrichment from only CCSN, and not from any longer delay-time sources like AGB stars or NSM, indicative of a very chemically immature and old star.

1.4.2 Interpreting Abundance Patterns

As stars of all sizes form and die, a variety of mechanisms alter their chemical compositions. An understanding of when and under what conditions these mechanisms occur can provide insight into how chemical evolution happens over time. But large numbers of stars, and therefore large numbers of enrichment events, can obscure signatures from individual events. In UFDs, the very small number of stars, and the

very short star-forming timescales make them a choice environment for detecting signatures of just a few, or maybe even one remarkable enrichment event. This makes it possible to compare stellar abundance patterns in UFDs to models of very early metal-poor and even metal-free supernovae, testing theories of early universe physics. Differing and localized patterns within UFDs can also provide insight into the dynamic histories of UFDs, possibly allowing for detections of very early galaxy merger events.

1.5 Thesis Objectives

UFDs are metal-poor, ancient, dark matter dominated galaxies that represent the floor of the galaxy mass function (Ricotti et al., 2008; Simon, 2019). They are thought to be relics of the first galaxies, and their stars preserve the signatures of early chemical evolution in the universe (Frebel et al., 2010a). Their unique chemistries can only be measured through analyses of high-resolution spectra. Much of their most interesting chemistry lies in the abundances of heavy neutron-capture elements, which have spectral lines primarily $<4000\mathring{A}$ (Roederer et al., 2022), a region which many spectrographs have little to no response in.

High-resolution studies of UFD stars have been conducted with high-resolution spectrographs such as UVES at VLT (Dekker et al., 2000), HIRES at Keck (Vogt et al., 1994), MIKE at Magellan (Bernstein et al., 2003), GRACES at Gemini North (Chene et al., 2014), and others. The GHOST spectrograph is a new instrument recently commissioned at Gemini South (Ireland et al., 2014; McConnachie et al., 2022b,a), designed to be a top-of-class "workhorse" spectrograph on an 8 m class telescope. Chapter 2 will introduce the GHOST spectrograph and its data reduction pipeline, and present the work completed during my internship at Gemini South.

It is possible that some UFDs have undergone mergers with other UFDs, creating extended halo-like structures in their outskirts. Identifying extended members is a challenge, since most membership algorithms strongly account for physical proximity, but it is also important to do so in order to maximize the number of stars providing data. The Bayesian inference method described in McConnachie & Venn (2020b) identified a number of new member stars in three UFDs, most of them at large half-light radii. Chapter 3 presents a detailed chemical abundance analysis of such extended member stars. The conclusions of my research and a summary of my internship work on GHOST are presented in Chapter 4.

Chapter 2

GHOST

From May 2022 until November 2022, I carried out an internship at the Gemini South telescope Observatory, in Chile. This internship was timed with commissioning of the Gemini High Resolution Optical SpecTrograph (GHOST).

In this Chapter, I will describe the GHOST spectrograph (Section 2.1.1) and its data reduction pipeline (Section 2.1.2). In Section 2.2 I present the work I completed during commissioning, and in Section 2.3 I describe my contributions (e.g. testing, calibrating, developing streamlining methods) towards completion and refinement of the data reduction pipeline. With this experience and related expertise, I also worked with the science team towards the goal of publishing the first science results which are described in Section 2.4, which also summarizes the work completed during my internship.

2.1 Introducing GHOST

GHOST is a fiber-fed spectrograph system that provides a strong signal in the blue end of the visual spectrum, with its simultaneous wavelength coverage from 348 - 1061 nm, and optimal performance between 363 - 950 nm. It can observe up to two objects simultaneously in a 7.5 arcmin diameter field of regard at R $\simeq$ 56,000 or a single object at R $\simeq$ 75,000. GHOST is equipped with hardware to allow for precision radial velocity measurements, expected to approach meters per second precision (McConnachie et al., 2024). An overview of GHOST is provided in Ireland et al. (2014); McConnachie et al. (2022b). More details on the Cassegrain unit and fiber system can be found in Zhelem et al. (2018, 2020); Churilov et al. (2018). For information on the optical bench design, refer to Pazder et al. (2016); Pazder et al. (2022). The precision radial velocity capabilities and data reduction pipeline are described in Ire-

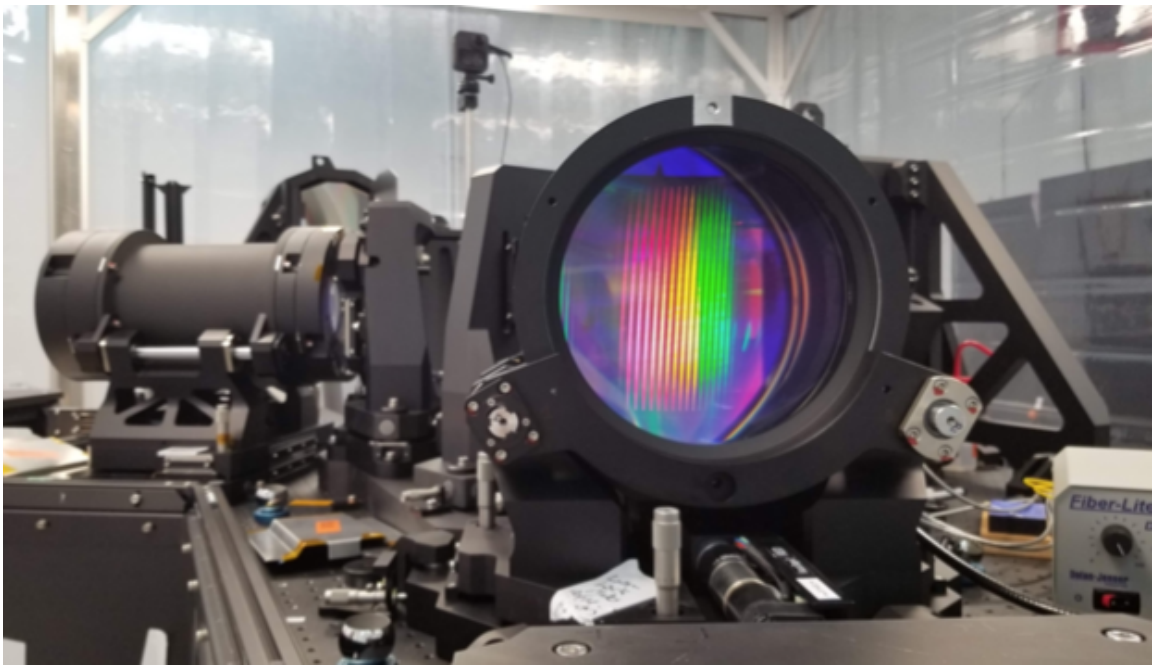

Figure 2.1: A view of GHOST taken during integration at Gemini South, taken from the location of the red detector looking into the red camera lens barrel as a white light source is injected into the system. Source: McConnachie et al. (2024).

land et al. (2016, 2018); Hayes et al. (2022). A complete overview of the scientific functionality and delivered science performance of GHOST using on-sky data can be found in McConnachie et al. (2024), and a forthcoming publication will present the science drivers of GHOST and its integration into Gemini operations (Kalari et al., in preparation).

2.1.1 Design

The following section 2.1.1 is a description of the physical design of the GHOST spectrograph. It is excerpted from the design summary in McConnachie et al. (2024), a publication which details the science performance of GHOST after commissioning. I am a co-author on the paper due to my contributions during commissioning.

GHOST consists of three primary components: the Cassegrain unit mounted on the telescope, the spectrograph bench located in the pier lab, and a fiber cable connecting the two. The Cassegrain unit contains the positioning arm system for two micro-lens based integral field unit (IFU) systems. The IFUs image slice (discussed further in section 2.1.1.a) a 1.2” aperture by either a factor of three in width using 7 fibers in the standard resolution mode or by a factor of five in width using 19 fibers

in the high resolution mode.

A 32 m fiber cable transports the light to the bench spectrograph that is located in a thermally stabilized enclosure in the Gemini Pier lab, and the fibers reformat the sliced image into a slit for injection into the spectrograph. Acquisition and guide fibers feed a guide camera for fine centering of the IFUs on the science targets at acquisition and during the exposure. A slit unit camera provides for active monitoring of the slit illumination during an exposure.

The bench spectrograph is a two arm, R2 echelle design. The beam is split by a high efficiency beam splitter which feeds the red and blue gratings and the respective camera optics and detectors. GHOST is designed so that the main science orders in the blue are m = 95 - 64, and the main science orders in the red are m = 66 - 34. In practice, however, additional orders are incident on the detectors which allows for expanded spectral coverage. Figure 2.1 shows a view of GHOST during integration at Gemini South, taken from the location of the red detector system looking into the camera as a white light source is injected into the system. The many orders of the red channel are clearly visible.

2.1.1.a Pseudo-slit and image slicing

In the cassegrain unit, light from an astronomical target is injected into microlenses at the end of an IFU fiber cable bundle. The sizes of each microlens array match the typical seeing disc at Gemini, and they have individual sizes corresponding to 0.4 or 0.25 arcsec on sky, for standard and high resolution modes, respectively. These segment the star image and set the spatial sampling of the fiber input.

Figure 2.2 shows the image-plane microlens configurations for heads IFU1 and IFU2. Each IFU head consists of three (IFU1) and two (IFU2) individual IFUs with a fixed configuration relative to each other. Everything in the left panel (IFU1) moves together on a single positioner, and everying in the right panel (IFU2) moves together on a single positioner. Thus it is possible to observe two science targets and sky simultaneously in standard resolution, or one target and sky simultaneously in high resolution.

At the output of the fibers (input to the bench echelle spectrograph), the object and sky fibers are reformatted into a pseudo-slit which is dispersed by the spectrograph. The microlens configuration (shown in Figure 2.3) is arranged in an imitation of a conventional slit so that the central microlenses at the IFU head which receive

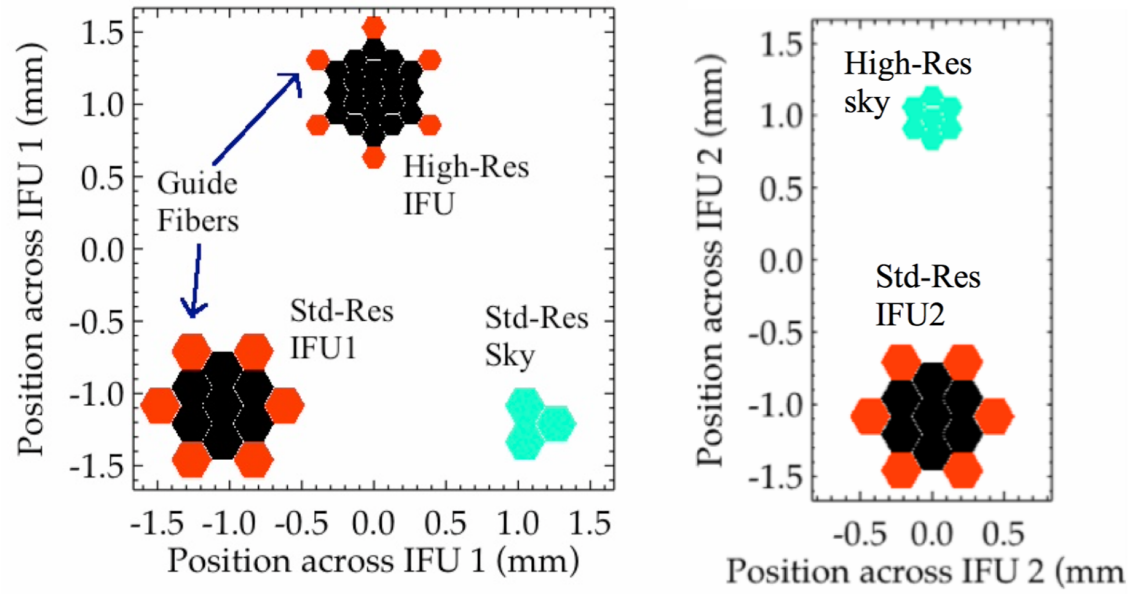

Figure 2.2: Arrangement of hexagonal microlenses in the image plane for IFU1 (left panel) and IFU2 (right panel). The image scale is 0.61mm/arcsec. Black hexagons correspond to the main science (target) regions; green hexagons correspond to sky regions; and orange hexagons correspond to acquisition and guiding fibers. Large hexagons correspond to the standard resolution mode, and small hexagons correspond to the high resolution mode. Source: Farrell et al. (2022).

the most flux in sufficient seeing maintain their central status in the pseudo-slit, creating the intensity profile shown in Section 2.1.1.e. Colors correspond to Figure 2.2. Also shown as a dark blue hexagon is the internal calibration fiber that can operate simultaneously with the high resolution observations.

2.1.1.b Slit Tilt

A generic feature of echelle spectrographs such as GHOST is that the slit (spatial direction) is not perpendicular to the columns (spectral direction) of the detectors, but instead rotates with wavelength. A change in alignment of the slit as a function of wavelength requires careful handling of the data in order to successfully extract the spectra. While the slit of GHOST does change in alignment with respect to the detector columns as a function of wavelength, the net rotation has been minimised. This has been achieved by optimising the tilts from individual components such that they have a net cancellation effect. The physical tilt of the slits are essentially vertical close to the center of the detector, and have a maximum of a 2 degree tilt either side

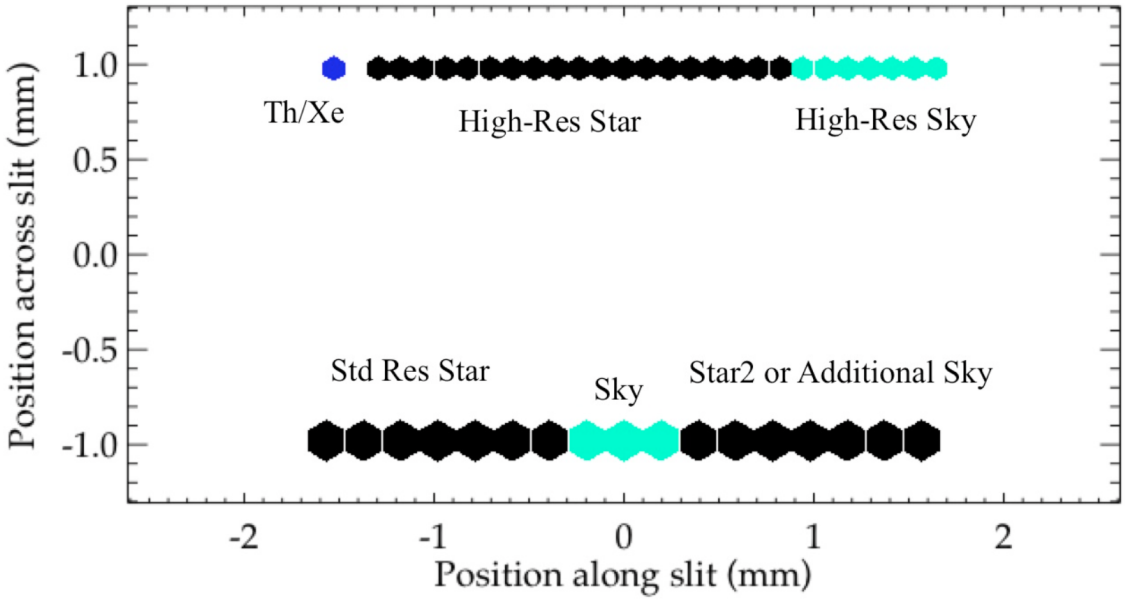

Figure 2.3: Arrangement of microlenses at the output of the fibers/input to the echelle spectrograph. The high resolution pseudo-slit is at the top, the standard resolution pseudo-slit is at the bottom. Also shown as the blue hexagon is the location of the microlens corresponding to the internal calibration source available in high resolution mode. Source: Farrell et al. (2022).

of vertical at the chip edges. This small tilt is accounted for in the data reduction pipeline, which is discussed in Section 2.3.2 and 2.1.2.a.

2.1.1.c Fixed Format

Figure 2.4 shows the global layout of the echelle spectra on the blue (left) and red (right) detectors. The design of GHOST is optimised for 363 - 950 nm (orders 95-36). However, photons spanning the range 348 - 1061 nm fall on the detectors (orders 98 - 32), with these wavelengths expected to be useful for science, at least for brighter targets. While these wavelength solutions are subject to small changes pending pressure variations and such, GHOST data is an effectively fixed format and is very stable.

2.1.1.d On-chip binning modes

A variety of on-chip binning modes are available for GHOST, in both the spatial and spectral directions, and are summarised in Table 2.1. Binning in either direction allows for a stronger signal to be obtained for the same exposure time, making

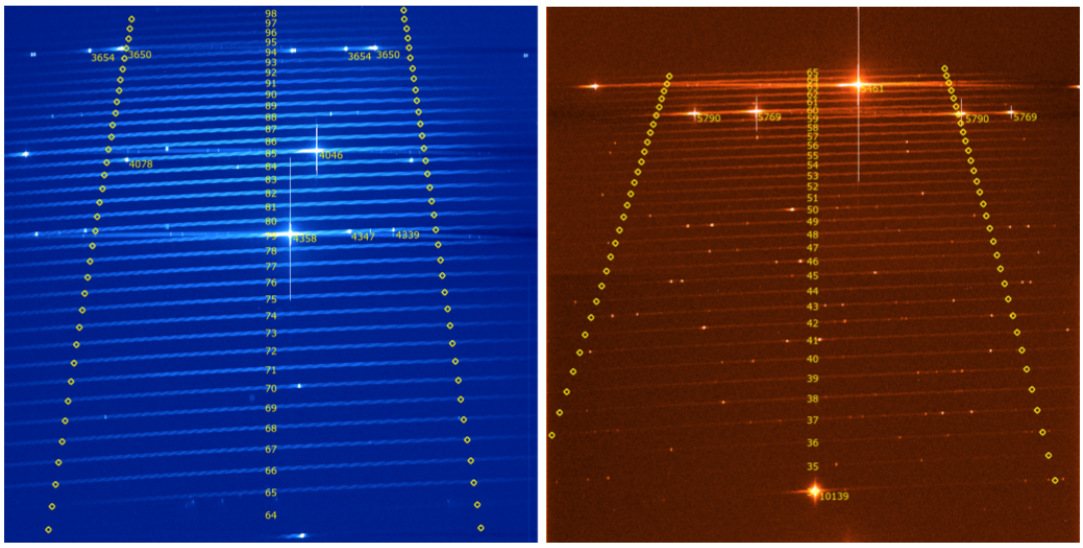

Figure 2.4: Full frame images from the blue (left panel) and red (right panel) detectors taken during integration at Gemini with light from a Hg lamp being fed down the standard resolution slit of IFU1. The wavelengths from some of the bright Hg lines are marked. Each order is labelled with its number, and the circles near the ends of the orders indicate the free spectral range. From McConnachie et al. (2023)

observations of faint targets cheaper in time. However, binning along the spectral direction reduces the resolving power of the spectrograph, so most binning adjustments are made in the spatial direction. Given that the slits are very nearly vertical everywhere, binning in the spatial direction leads to virtually no change in the spectral resolution, but can be highly beneficial for increasing the SNR of faint objects. Binning in the spatial direction will merge some of the sky flux into the object flux, which may be beneficial if the sky noise is small enough.

2.1.1.e Slit Viewer Camera

GHOST has a slit viewer camera that images the output of the slit in blue and red light. Specifically, the beam from the spectrograph pseudo-slit enters the spectrograph via reflection from a custom beamsplitter. This beamsplitter transmits 1% over all wavelengths, and the transmitted beam is imaged by a dedicated slit-viewing CCD camera in two wavelength bands (blue, 430 – 600 nm; red, 600 – 750 nm). The image of the blue and red beams can be seen in Figure 2.5. The exposure time for this camera is set independently of the science exposures, and can be as short as 0.1 seconds. The slit-viewing camera has multiple uses. Possibly its most important use

Table 2.1: Main configurations of GHOST in terms of delivered spectral resolving power for different on-chip binning options, as measured for even illumination of the slit. These should therefore be considered lower limits to values obtained when targeting on-sky point sources. Values in parentheses are those obtained assuming spectral resolving power is set by detector pixel sampling. Source: McConnachie et al. (2024)

IFU option	On-chip binning spectral x spatial	Effective spectral resolving power	Notes
Standard	1x1	56K	oversampled
Standard	2x2	56K (46K)	good default mode
Standard	2x4	56K (46K)	for faint objects
Standard	2x8	56K (46K)	for faint objects
Standard	4x4	(23K)	lowest resolution
High	1x1	75K	PRV observations
High	1x2	75K	Good default mode
High	1x4	75K	for fainter objects

is during the data reduction process (Ireland et al., 2016; Hayes et al., 2022). The blue and red slit-viewing images closely correspond to the wavelength ranges of the blue and red science images, and they therefore provide an accurate measure of the flux distribution in the spatial direction for the optimal extraction of the science spectra.

2.1.2 Data Reduction Pipeline

The following section 2.1.2 summarizes the design of the data reduction pipeline for GHOST. It excerpts from a paper I co-authored and presented a poster on at SPIE 2022 (Hayes et al., 2022) shortly after the first commissioning run.

The data reduction software for GHOST (GHOSTDR) is the first instrument pipeline to be developed specifically for DRAGONS (Labrie et al., 2019) (Data Reduction for Astronomy from Gemini Observatory North and South), a python-based framework operating within the AstroConda environment. The core component of DRAGONS is the Recipe system, which is designed so that every image type (e.g., bias, dark, flat, arc, object) has an associated "recipe", i.e., a list of processing steps referred to as "primitives". The DRAGONS Reduce class automatically identifies the correct recipe for each image that is provided and processes it accordingly. This combined with the DRAGONS calibration database manager "caldb" will search for the appropriate calibration frames (biases, darks, flats, etc.) and supply these to the

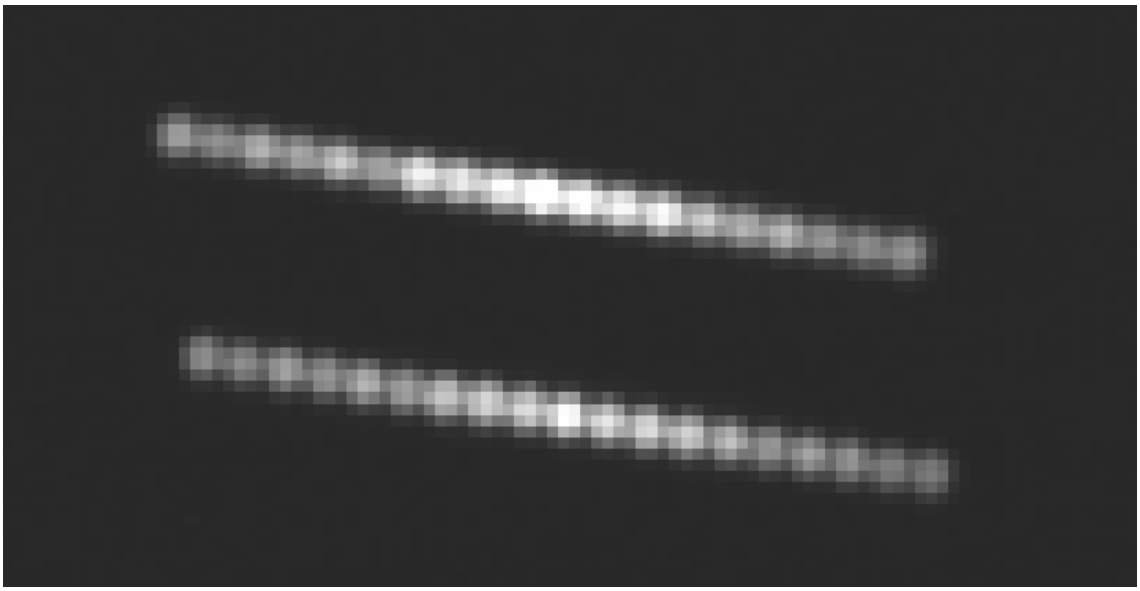

Figure 2.5: A binned 2x2 slit viewer camera frame of the red (top) and blue (bottom) detectors showing the pseudo-slit for a star observed in 0.7 arcsec seeing. The reassembled high resolution IFU mode produces a tapering along the pseudo-slit due to the hexagonal ring-like distribution of the fibers at the IFU. Source: Hayes et al. (2022).

necessary primitives in the data reduction process. Combined, the recipe system and the calibration database mean that minimal user interaction is required to perform the basic data reduction steps.

GHOSTDR is an open source code[1] built on the above framework. Figure 2.6 shows a flowchart of how various images are processed by the recipe and primitive framework. While some primitives are standard in the DRAGONS system (e.g., bias and dark subtraction), GHOSTDR includes several primitives that are specific to the reduction of GHOST spectra. These include primitives such as order tracing and mapping of the integral field unit pseudo-slit onto the detectors, performing 2D extractions, fitting the wavelength solution, interpolating and order combining the extracted spectra, and optional capabilities such as determining the barycentric correction and response corrections with a spectrophotometric standard star.

[1]The GHOSTDR pipeline is available at `github.com/ANU-RSAA/GHOSTDR`

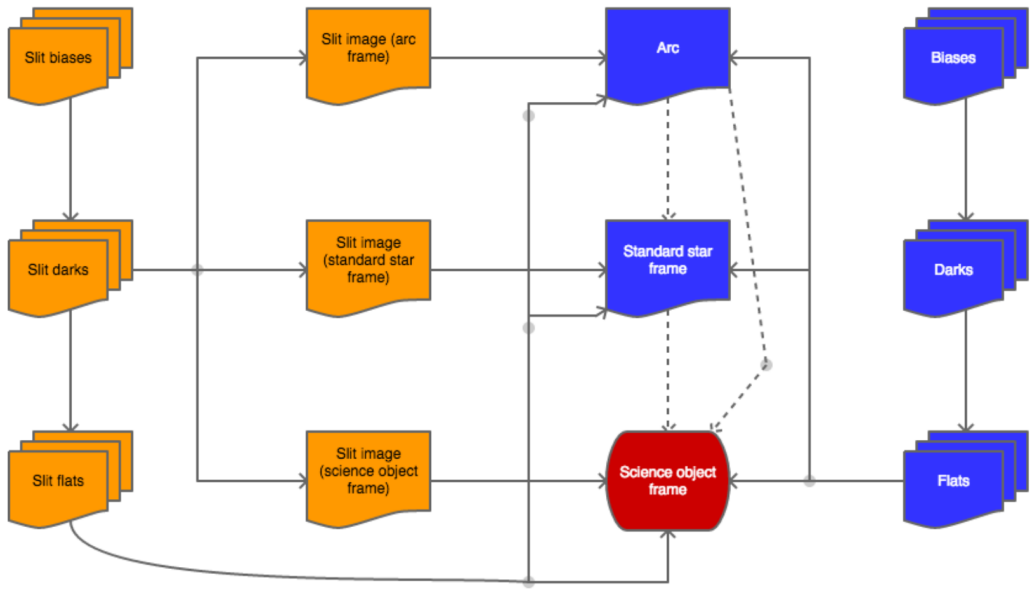

Figure 2.6: GHOSTDR processing flowchart managed by dedicated recipes for each image type. Slit viewer camera images are noted in orange, calibration frames are identified in blue and science frames are shown in red. Solid arrows show required data processing steps that use each of the identified images, whereas the dashed arrows show optional data processing steps that use GHOSTDR data products rather than raw or processed images. Source: Farrell et al. (2022).

2.1.2.a Polynomial Models

For the order tracing, extraction and wavelength solution, GHOSTDR is built on a polynomial model of the spectrograph (Ireland et al., 2018), which maps several quantities – the order trace, wavelength mapping, slit magnification in both spectral and spatial directions, and slit rotation – as a polynomial function of both order number and pixel number in the spectral direction. Due to the instrument's stability (Pazder et al., 2020), these models are expected to vary by only small amounts from night to night. Thus, default instrument models can be produced by an initial examination of high quality calibration frames and used as a starting point for the GHOSTDR reduction system to automatically perform fine tuned adjustments using nightly calibrations for science quality data reduction.

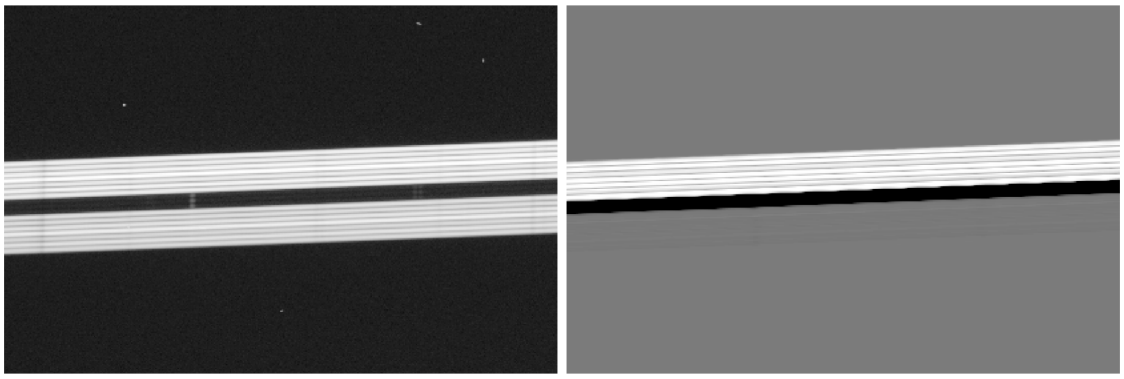

Figure 2.7: A portion of the red camera observation of a pair of stars (left), and extraction weights for Object 1 (right). Left: The traces of the Object 1 IFU (top), sky IFU (middle, darker), and Object 2 IFU (bottom) are shown with 1x1 binning. The individual fiber traces (∼horizontal) can be seen of the pseudo-slit (vertical). A few bright sky lines can be seen between the two object spectra from the sky fibers. Right: the extraction weights for the Object 1 IFU fibers. White show pixels with positive (scaled) extraction weights identifying the object spectrum, gray shows pixels where the extraction weights are zero, and black show pixels with negative (scaled) extraction weights, in particular tracing the sky fibers, which are used for a sky subtraction. Source: Hayes et al. (2022).

2.1.2.b Slit Viewer Camera

Another unique aspect of GHOST is its slit viewer camera, which monitors the illumination of the slit over the duration of an exposure. This can then be used as an exposure meter, providing a photon-weighted mean exposure epoch, and when averaged over the full exposure time, provides a direct measure of the slit profile to optimize the spectral extraction. Figure 2.5 shows an example of a slit viewer camera image of an object observed with the high-resolution IFU. The fibers are organized into a pseudo-slit, which unpacks the fibers from the IFU such that the central IFU fiber is in the center of the pseudo-slit. The inner ring of 6 IFU fibers are split 3 and 3 on either side of the central fiber along the pseudo-slit, and the outer ring of 12 IFU fibers are again split on either side along the pseudo-slit. Figure 2.5 shows a star in 0.7 arcsec seeing, where the PSF is resolved with a 1.2 arcsec diameter on the IFU, and when reassembled as a pseudo-slit, then the profile produces a slit illumination that tapers outward from the central fiber.

2.1.2.c Spectral Extraction

Combined, the slit viewer camera images and the polynomial models of the spectrograph allow GHOSTDR to calculate optimal extraction weights needed to perform the 2D extraction. This accounts for the details in the slit profile (e.g., slit rotation), and is motivated by the design of GHOST. For example, the fiber pseudo-slit extraction weighting is necessary to identify the traces of fibers from each of the object and sky IFUs. As seen in Figure 2.7, the trace of the fibers in the pseudo-slit are tightly packed, but with slight gaps in illumination, which is a unique challenge for the extraction. In addition, the variety of possible observing modes – one or two object in standard-resolution, single object high-resolution, and precision radial velocity in high-resolution with a simultaneous internal ThXe arc lamp, as demonstrated in Figure 2.9 – must be handled by the data reduction pipeline and each requires precise knowledge of the slit profile. Thus, with the slit profile known (from the slit viewer camera) and a stable model of the location of the IFU traces, GHOSTDR can calculate extraction weights for each of the object and sky IFU fibers along the pseudo-slit.

The right panel of Figure 2.7 illustrates the result of one of these calculations, highlighting the extraction weights with sky subtraction for one of two objects observed in the standard mode. GHOSTDR is able to accurately identify the trace of the object IFU fibers (and the sky IFU fibers), and weight the extraction such that the central pixels of each fiber are weighted more strongly which reflects that they are more illuminated. This reduces noise, which is particularly important for observations of fainter targets – one of GHOST's key science requirements.

The pipeline offers multiple versions of the extraction, extracting objects from either IFU 1, IFU 2, or both, where any combination can include or ignore sky subtraction. For example, sky subtraction is necessary for deep observations of faint targets, but only adds noise for short exposures on bright targets. The reduction process generates intermediate data products along with their pixel variances and bad pixel maps. As a final data product, GHOSTDR returns two versions of the extracted 1D spectra for each camera: (i) order-by-order instrumental flux, and (ii) interpolated and order combined fluxes for each of the objects in the IFUs (and the sky IFU), along with the associated variances and wavelengths. The pipeline also provides the 2D pixel extraction weights for each IFU, which can be inspected for quality assurance purposes.

2.2 Commissioning

GHOST was successfully commissioned at Gemini South in 2022 (McConnachie et al., 2022b). I performed tasks necessary for commissioning during the first and second runs on June 20-30, 2022 and September 12-15, 2022. Such tasks included target selection, log-keeping, exposure-time calibration, and instrument operation. In the following section I will discuss how my work on these tasks contributed towards the commissioning and operation of a brand new workhorse spectrograph at a world-class observatory.

2.2.1 Target Selection

Target selection for an instrument commissioning requires special considerations beyond what is needed for a regular science observation. The main priority is to thoroughly test the instrument, until failure if possible. Scientific value is an added bonus. Aspects of the instrument that were important to test include, but are not limited to, all moving parts, sensitivity, wavelength stability, the various observing modes (HR vs SR, dual vs single acquisition) guiding modes, and the instrument-telescope interface. It was also important to obtain observations of industry standard stars—those which have been observed in great detail by many other observatories. Comparing against standards catalogues allows us to directly compare performance with similar instruments. Aside from standard stars, the nature of the stars we observed were not critical to the tests conducted, so it was desirable that scientifically interesting stars were targeted wherever possible. To achieve this, we created a list of stars with comprehensive sky coverage at a variety of magnitudes and colours with some sort of scientific potential.

We collected lists of standards which were relevant to the science we wanted to do (RV standards, metal-poor standards), and then had to determine which were available for observing. We discarded all declinations greater than Gemini's northern limit of 15 degrees, and we discarded all right ascensions not seasonally visible at night, between roughly 20 and 180 degrees. The remaining stars were arranged into testing categories, and sorted by right ascension and magnitude. Because it could not be guaranteed when any given test would be performed, having the ability to easily select visible and relevant stars from a list at any time of the night meant more attention could be paid to the testing at hand.

However, unusually adverse weather conditions limited our choices beyond expec-

tation. For the majority of the commissioning in June, the observatory encountered weather conditions which would have normally cancelled any observing for the night. High winds flowing from the north/north-west meant the dome must maintain a southward pointing, restricting the sky to only the southern-most targets at declinationsf of -40 degrees or lower. Thick but not completely opaque cloud cover created as much as 8 magnitudes of light extinction. Given that GHOST was designed to see down to G$\sim$19, many of our scientific targets were G=16 or fainter. In order to get a signal through the cloud cover, some G$\simeq$8 standards and even brighter were observed. On the first night, I searched beyond our curated list for any available very bright stars, finding targets which under ordinary conditions would have been too bright for the instrument to view at all. But in such harsh weather conditions, such a bright star was just enough to accomplish the first basic tests before snowstorms shut the telescope down completely the following nights.

Another complicating factor was that any observing target needed to have another bright star within 7 arcmin for the telescope to guide on. As such, pairs and sometimes even triples of bright stars were needed. Dr. Trystyn Berg provided me with a python script[2] which combed through the Gaia database to find pairs of stars which met our previously listed requirements. I used that script, accounting for the adverse weather conditions, to find triples of stars which were used to test the dual-acquisition modes of GHOST.

After a week of storms, we finally had a couple good nights of weather, and were able to prioritize targets with scientific value. However, the Milky Way was passing through zenith close to the middle of the night, and many of our desired targets were pointing away from the disk. Prioritization choices needed to be made for the crowded observing at the start and end of night. I ensured that HD122563 was selected over other early-evening targets, as it is a crucial benchmark in the study of metal-poor stars. Analysis of GHOST observations of HD122563 is done in Hayes et al. (2023).

We wanted to test one of GHOST's key use cases: observing two stars in a nearby ultra-faint dwarf galaxies simultaneously, and a dearth of targets during the middle of the night meant that some very long exposures could be completed without significant time trade-offs. Referencing new targets found by the algorithm detailed in Jensen et al. (2024), we selected two stars in the UFD Aquarius II (Zaremba et al., 2024 in prep), which had not previously been a high priority, but would be the first HR

[2]Pair-finder script is is available on my github at github.com/wallerf/ghostdr_tools/blob/main/mk_acq_pairs.py

spectra obtained from this galaxy.

Also selected were a number of previously unobserved stars in Tucana II, of increasing faintness. This tested the limits of what was possible with GHOST sensitivity, to great success. The mood in the control room was nothing short of celebratory when, after a 15-minute acquisition with a maxed-out exposure time, GHOST succeeded in guiding on a magnitude 19.7 star. A 15 minute exposure yielded spectral lines albeit with very low S/N, so GHOST should be able to obtain HR spectra of stars fainter than previously possible. Such exposures would take many hours, and the acquisition alone is a large time-expense, but for the right target with a high scientific potential, GHOST is able to obtain spectra where other spectrographs may not.

2.2.2 Logkeeping

I was the primary logkeeper during the commissioning. This involved keeping track of the time of events along with brief descriptions. I noted what targets were being observed and when, the bugs that arose, and any thoughts or ideas that we might want to revisit later. At the end of the night, the logs were revisited to identify all the bugs, and a plan was made for how the daytime software team or instrument team might best address them before the next night.

I also kept the observation log, which involved filling out a spreadsheet with the names of targets observed and all relevant details such as exposure times, modes, magnitudes, locations, and notes about any problems that might have occurred. These logsheets proved invaluable for the team working on the data reduction, because the instrument was not yet interfacing properly with some of the telescope systems. Any of the resultant missing or hidden tags of importance could be recorded in the logsheets and referenced during data reduction.

2.2.2.a Testing Calibration Lamp for Precision Radial Velocity

Many of the design choices made for GHOST also make it a a tool able to do precision radial velocity (PRV) measurements. Towards this end, a simultaneous calibration source (ThXe) for use in the high spectral resolution mode was installed. The source is very bright, and even a brief exposure can result in a large number of saturated (Xe) lines in the red camera. However, the lamp has its own selection of neutral density filters which can reduced the number of saturated lines. From single exposures of the source with each filter, I identified lines close to saturation, and extrapolated the

Table 2.2: Exposure times for the ThXe lamp when used in conjunction with the neutral density filters, to prevent oversaturation of the lines. These times are indicative only and will need to be refined over the lifetime of GHOST. Source: McConnachie et al. (2024) where it was coallated from my own original work.

	Max Exposure Time (s)	
ND Filter	Blue	Red
clear	1	1
0.5	1	1
1	1	1
1.5	5	1
2	15	3
2.5	90	10
3	150	15
3.5	1000	45
4	2500	120
5	> 3600	300

longest exposure possible while limiting the number of saturated lines. These results are summarized in Table 2.2, where a maximum exposure time is provided for the use of each filter. During a science observation, the exposure time would be selected for the target, and an appropriate filter would be chosen using this table to minimize saturated pixels.

2.2.3 Slit Viewer and Guide Cam empirical exposure chart

One of the challenges during the commissioning was quickly setting the slit and guide camera exposure times. For an observing proposal, this task would typically be performed ahead of time. During commissioning, because of our rapidly changing weather conditions, and consequently often changing targets, we had to estimate during an observation set up. Under or over-exposed images would reduce the function of these cameras, so accurate estimates are important. The estimates and adjustments made during the first commissioning provided an empirical relationship between exposure times and target magnitude. I interpolated the trend in this data, shown in Figure 2.8, and created a table of suggested slit and guide camera exposure times at every half-magnitude. This table saved time in the September commissioning and was provided to the Gemini GHOST team for future use.

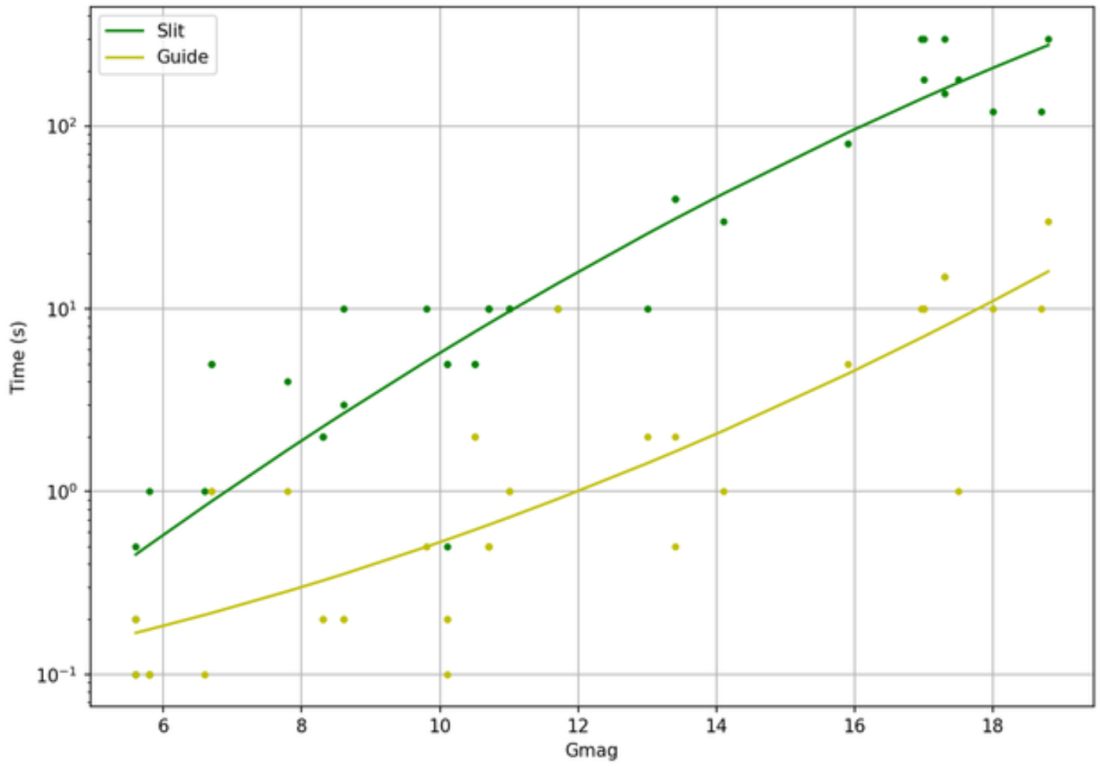

Figure 2.8: Green and yellow points show chosen exposure times for the slit and guide cameras per target magnitude. An interpolated trend is shown for each camera. This interpolation informed future exposure time selections based on target magnitude. This figure is original work created from logbooks I kept during commissioning.

2.2.4 Operating GHOST

I operated the GHOST instrument for the latter half of one night during the second commissioning run, when the instrument scientist left suddenly. Guided by the instrument and science team who were participating remotely, I used the engineering console to queue up planned observations. This included testing a bug causing failed acquisitions, a successful science exposure, a routine acquisition of a standard star, and running the morning calibrations. Despite being the sole person in the observer room, I was able to minimize time lost and also contribute to the early science-quality data acquired.

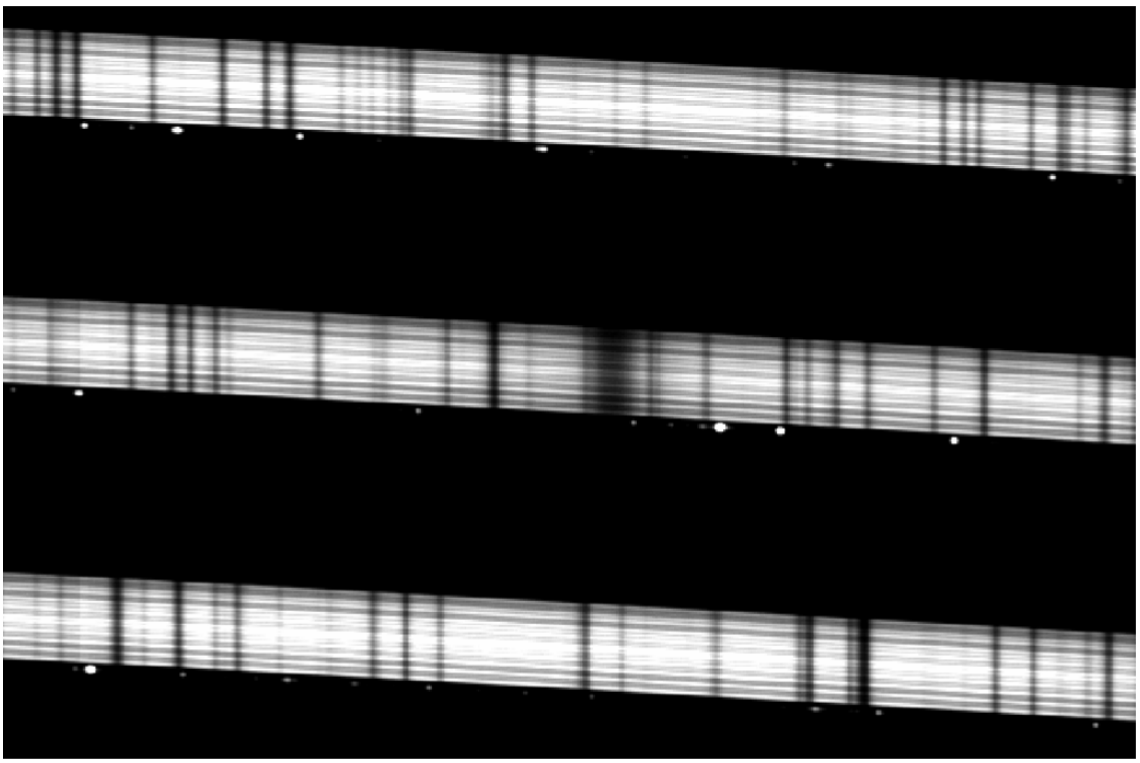

Figure 2.9: A zoomed in portion of orders 70-72 (from bottom to top) in the blue camera centered around the Hβ absorption line for a star in the high-resolution IFU, observed simultaneously with a fiber connected to an internal ThXe lamp (the lower fiber in each order, noticeable as the only emission lines). These can be used for simultaneous wavelength calibration and precision radial velocity measurements. Source: Hayes et al. (2022).

2.3 GHOSTDR Testing

One of my tasks at Gemini was testing the data reduction pipeline for GHOST with the first on-sky data. I bug tested, created organizational data systems, and refined some parameters which were previously set by testing from synthetic data.

Once the first on-sky data was taken at the first commissioning run, it was time to start testing the GHOSTDR pipeline (Ireland et al., 2018; Hayes et al., 2023). Previously, it had been tested only on synthetic data. Testing on real on-sky data revealed bugs in the instrument-telescope interface systems, and provided data necessary for refining the polynomial models in the pipeline.

Some examples of smaller bugs that were addressed include:

- adding the ability to stack arc frames

- identifying dead pixels and hot pixels and masking them
- identifying which files the calibration manager was not able to find
- correctly applying mean vs median stacking techniques when stacking multiple frames of a calibration or target exposure.

Many of these were found in the simple process of trying to produce any kind of extracted spectra, and others were found while trying to produce better polynomial models. Bug testing is a fiddly process that involves repeating the same actions over and over. Because of this, some effort goes towards streamlining the process as much as possible. I will discuss a couple systems I designed to expedite the testing process in Section 2.3.1, and will follow that up in the Section 2.3.2 by discussing the main problem I was solving.

2.3.1 Streamlining Workflows

I built an On-Chip Visualizer tool[3] to aid with the visualisation of the detectors and the spectra captured on them. A user could select a wavelength range to output an image of the corresponding sections on the detector. Figure 2.10 shows an example of the visual output. The top panel shows the extracted 1D order-by-order spectrum of the emission from a ThAr arc calibration lamp. A user can scroll through the spectrum to select features, for example some of the calibration lines are indicated by black solid triangles. Two orders contribute to the flux, the red with full coverage over the panel, and the purple with only 3/4 coverage. The bottom panel shows cut-outs of the chip where the first image corresponds to the purple order, and the second to the red. They are lined up by wavelength so the spectral features are aligned vertically. The slit tilt (previously introduced in Section 2.1.1.b) at the edge of the purple order can be seen in the angle of the spectral lines, but it does not produce a noticeable effect in the extracted 1D spectrum because the slit tilt is correctly modelled in this extraction.

The On-Chip Visualizer is compatible with any calibration frame: bias, dark, flat, arc, or object, and also all of the intermediate data products created by GHOSTDR, for example the extraction weights assigned to each pixel. It was a powerful tool for

[3]Can be found as 'GHOSTDR_tutorial_3.2_seeWavelengthOnChip' in the GHOST Tools repository available at github.com/wallerf/ghostdr_tools/

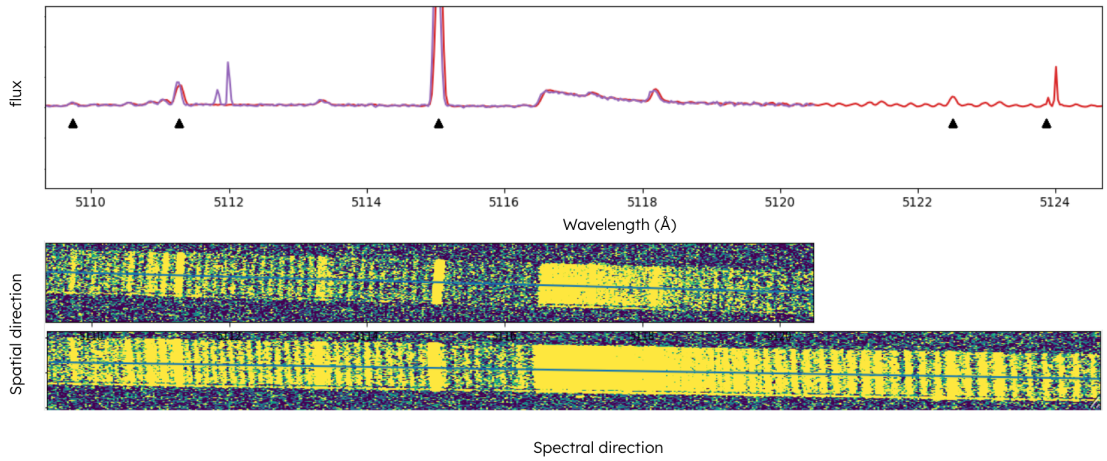

Figure 2.10: A range of wavelengths is shown in both the 1D (upper) and 2D (lower) spectra of a ThAr calibration arc. The 2D regions show the exact pixels on the detector which contribute signal to the 1D spectra, where bright yellow is high flux and dark blue is low flux. Two 2D regions are shown, because two orders, purple and red, overlap in this range. Solid triangles indicate spectral lines for which we had precise calibration data, and which were used to calculate the wavelength solution. Original image created using the On-Chip Visualizer tool.

understanding the behaviour of the GHOSTDR pipeline and expedited bug diagnoses in many instances.

2.3.2 Wavelength solution and calibration

While the wavelength solution is still subject to small changes environmental variations, GHOST data is an effectively fixed format due to the instrument's temperature and pressure stability. The GHOSTDR pipeline can fine-tune a default wavelength solution using nightly calibrations to account for small variations. Generating a robust default model was no small task, requiring careful calibration-line curation and a lot of iteration, as discussed below.

GHOSTDR calculated a new wavelength solution for in every object reduction using ThAr arc calibration frames taken at the beginning and end of the night. Using a list of hundreds of Th and Ar emission lines and an initial wavelength solution estimate, GHOSTDR would make Gaussian models of emission lines and then calculate the residuals between the expected and modeled wavelength of each line. Small changes would be made to the model, and the process repeated until the residuals were minimized. Incorrectly identified lines could skew results between orders. A

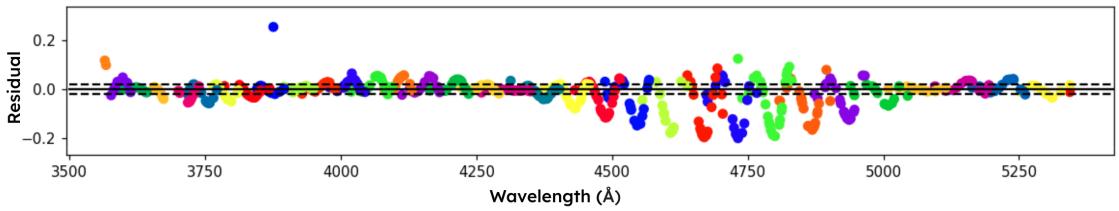

Figure 2.11: In this residual chart I show an example of a poor wavelength solution. Each coloured point is the residual between the calculated line wavelength and expected wavelength for every ThAr spectral line with atomic data in the red camera. Colours indicate separate orders. Solid line is at zero residual, and dotted lines above and below show the acceptable mean residual amount for a good wavelength solution.

manual examination of the residuals could provide clues as to where a problem stems from, as can be seen in Figure 2.11. The single point with a high residual below $4000\mathring{A}$ indicates a misidentified line, while the curving structures around $4750\mathring{A}$ indicate an error in the initial model which could not converge correctly. Upon seeing such curving patterns in order-by-order residuals, a visual inspection of the 1D spectra was often necessary, for which the visualization tool described in Section 2.3.1 proved invaluable. Improper slit tilt modelling also caused skew between orders, as can be seen in the 1D spectrum in Figure 2.12. The green and blue orders grow increasingly skewed with decreasing wavelength, and the lines in the green order are much shorter and wider than in the blue as a result of the slit tilt model assigning improper extraction weights to pixels.

Identifying these problems, and curating a list of reliable spectral lines made it possible to generate a default wavelength solution which performed reliably on spectra taken on many different nights. With an appropriate wavelength solution, the orders could be combined into one long 1D spectra, improving the S/N where orders overlap, and the spectrum would be ready for analysis.

2.4 Summary of Internship Work

In the summer and fall of 2022, I carried out an internship at the Gemini South telescope Observatory, in Chile. This internship was timed with commissioning of the Gemini High Resolution Optical SpecTrograph (GHOST).

Since commissioning, GHOST has been integrated into the Gemini instrumentation suite. The Observatory has conducted an extensive System Verification process during which time the end-to-end processes and hard-ware associated with GHOST,

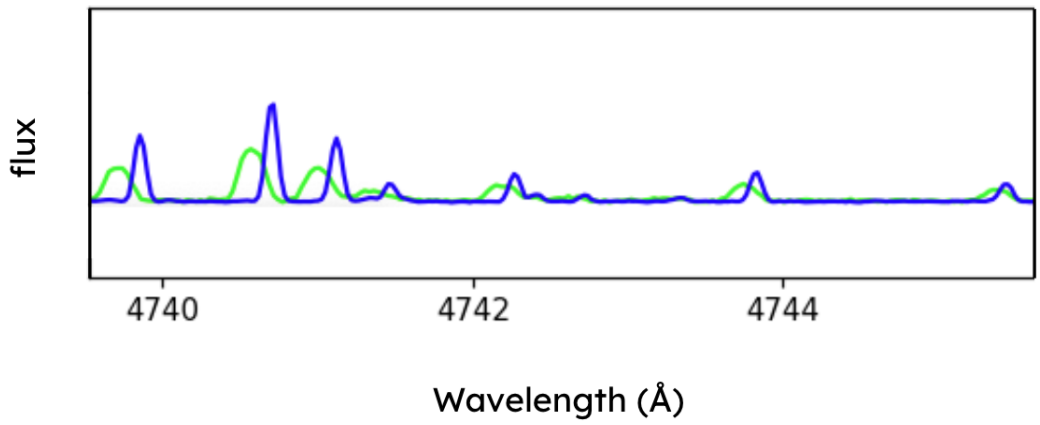

Figure 2.12: Two overlapping orders where blue is from a central region of its order, and green is at the edge of its order. The line-spreading effect in the green show the result of the a poorly modelled slit-tilt. From right to left, I show that the orders become more and more misaligned.

from proposal submission through to data reduction, were tested and de-bugged.

During this internship, I utilized skills I had already developed in analyzing high-resolution stellar spectra, and expanded my skill-set by applying them to instrumentation and data pipelines. I contributed to 17 nights of commissioning between June and September, and spent the following months as one of the first to process data using the data reduction pipeline. I performed bug-testing and developed streamlined methods for processing data to work towards completion and refinement of the data reduction pipeline. With this experience and relative expertise, I worked with the science team towards the goal of publishing our first science results.

The first science results from GHOST, obtained using commissioning data, were presented in Hayes et al. (2023); Sestito et al. (2024); Dovgal et al. (2024). I am co-authors on all of these papers due to my contributions during commissioning.

Chapter 3

The Cosmic Hunt

The following chapter contains a paper published in the Monthly Notices of the Royal Astronomical Society volume 519, pages 134-151 (Waller et al., 2023) and comprises the bulk of the research in this Masters of Science thesis. I was the first author and leading contributor, including all of the chemical analysis of the spectra that were taken at the Gemini North telescope with this GRACES spectrograph. This included two different kinds of analyses including independent errors analyses for both methods. I made all of the tables and plots in the paper, which included an extensive review of chemical abundances from previous analyses for the three target UFDs.

3.1 Introduction

Dwarf galaxies are among the oldest and least chemically evolved objects in the universe (e.g., Tolstoy et al., 2009; Bullock & Boylan-Kolchin, 2017b). They include the most dark matter dominated systems known, the ultra-faint dwarf (UFD) galaxies, which are defined as galaxies with absolute magnitudes $M_V > -7.7$ ($L < 10^5 L_\odot$; Simon 2019). Their dynamical mass-to-light ratios (M/L) reach 100-1000, and metallicities are less than 1% solar (McConnachie, 2012; Simon, 2019). Such systems provide interesting challenges and unique opportunities for testing our understanding of dark matter, and for studying the dark energy plus cold dark matter (ΛCDM) cosmological paradigm. In addition, recent hydrodynamical simulations of low mass galaxies embedded in dark matter halos have shown that star formation is quenched at very early times, consistent with quenching from cosmic reionization (Wheeler et al., 2019; Applebaum et al., 2021). This is similar to the reconstructed star-forming histories found for some UFDs (Brown et al., 2014; Bechtol et al., 2015), suggesting that UFDs

are possibly the modern day relics of the earliest galaxies. The relatively unevolved nature of UFDs make them ideal objects to provide insights into galaxy formation and nucleosynthetic events in the early universe.

Simulations also suggest that the Milky Way (MW) halo has grown from the accretion of these small systems (Bullock & Johnston, 2005; Starkenburg et al., 2017a; El-Badry et al., 2018), providing another way to find and study UFDs – as disrupted, coherent metal-poor structures, *i.e.*, stellar streams. The exquisite data from the Gaia satellite (Gaia Collaboration et al., 2018a) has uncovered many new structures in the MW halo (Martin et al., 2022b; Li et al., 2022). As UFDs are by definition extremely faint systems, with only a handful of stars that are bright enough for detailed analyses (McConnachie, 2012; Simon, 2019; McConnachie & Venn, 2020b), chemo-dynamical studies have been hindered by cosmic variance and stochastic sampling. For example, combining Gaia DR3 data, spectroscopy, and direct dynamical modelling over a large extent (4.1 half-light radii) in Boo I, Longeard et al. (2022) has found that this UFD is more elongated than previously thought and may have been affected by tides, thereby strengthening links between nearby UFDs and stellar streams in the MW halo.

Nevertheless, while some of these streams appear indeed to be remnants of accreted dwarf galaxies (Ibata et al., 2001, 2021; Thomas & Battaglia, 2022; Li et al., 2022), others are most likely disrupted globular clusters (Malhan et al., 2019; Martin et al., 2022a; Li et al., 2022). Distinguishing streams that originate from UFDs or globular clusters is greatly helped by detailed chemical abundances from high resolution spectroscopy. Massive, old globular clusters will show variations in their light elements (CNO, Na, Mg, Al; Carretta et al., 2009; Bastian & Lardo, 2018) attributed to contributions from multiple populations of stars. In UFDs, the location and specific properties of supernovae and compact binary merger events can impact which stars become enriched and by how much (Leaman, 2012; Nomoto et al., 2013; Reggiani et al., 2017; Kobayashi et al., 2020b). Thus, the specific abundance ratios of a variety of elements can provide clues to the characteristics of the initial star formation events, whether streams are disrupted globular clusters or UFDs.

Most UFD stars with detailed analyses are bright (V<19) and situated close to the projected UFD centres. Yet—recently several candidate members stars have been found at very large half-light radii (R_h) (McConnachie & Venn 2020b; Pace & Li 2019), where R_h is the radius within which half of the galaxy's light is contained, measured along the semi-major axis. This includes one star in Tuc II at $\sim 9\ R_h$, which demonstrates that Tuc II is remarkably extended as a result of either strong bursty

feedback, an early galactic merger, or tidal interactions with the MW halo (Chiti et al., 2021). Coma Berenices (Com Ber) is a similar UFD to Tuc II, with an old age from stellar isochrones, low metallicity from spectroscopic analyses, and candidate members located at large half light radii, $> 4R_h$ (e.g., Frebel & Bromm, 2012; Brown et al., 2014; McConnachie & Venn, 2020b). Three stars in Com Ber have surprisingly low heavy element abundances; in particular, their s-process abundances (Y, Sr, Ba, Ce) are all lower than known stars of similar metallicity in the MW halo ([Fe/H] ~ -2.5; Frebel et al. 2010a). This unique chemical fingerprint has been interpreted as a result of enrichment by a single metal-poor supernova event (> 20 $M_\odot$), with little to no later chemical evolution. This interpretation would make Com Ber a relic from early times, where only one stellar generation may have formed after the first, Population III, SN explosions (Frebel & Bromm, 2012).

Other UFDs have shown very different chemical evolutionary patterns. Spectroscopic studies of stars in Reticulum II (Ji et al., 2016; Roederer et al., 2016) and Tucana III (Hansen et al., 2017) have shown a mixture of r-process normal and r-process rich stars, which is interpreted as a result of stochastic sampling and late enrichment from a rare neutron-binary merger (like GW170817; Tanvir et al., 2017b). The large variation in abundance patterns inferred from only a handful of stars in each UFD shows why it is necessary to observe as many bright stars in these systems as possible, to overcome cosmic variance effects and to derive further constraints on nucleosynthetic sources, progenitor masses, chemical yields, gas mixing, and stochastic sampling (Su et al., 2018; Wheeler et al., 2019; Kobayashi et al., 2020b; Applebaum et al., 2021). In this way, UFDs can provide unique information on star formation properties and on the origins of the elements at the earliest times.

In this paper, we add to the canon of high-resolution spectral analyses of bright stars associated with UFDs. We present the analysis of five stars in three UFDs; Coma Berenices (Com Ber), Boötes I (Boo I), and Ursa Major I (UMa I). Targets were selected with high probability memberships but at large half-light radii (see Section **??**). Observations and spectral data reduction are described in Section 3.3. Stellar parameters for the model atmospheres analysis are discussed in Section 3.4. Spectra were analysed using both spectral line equivalent widths and spectrum synthesis fitting in Section 3.5. Chemical abundances are discussed in Section 3.6 and placed into the context of the evolutionary history of each UFD in Section 3.7.

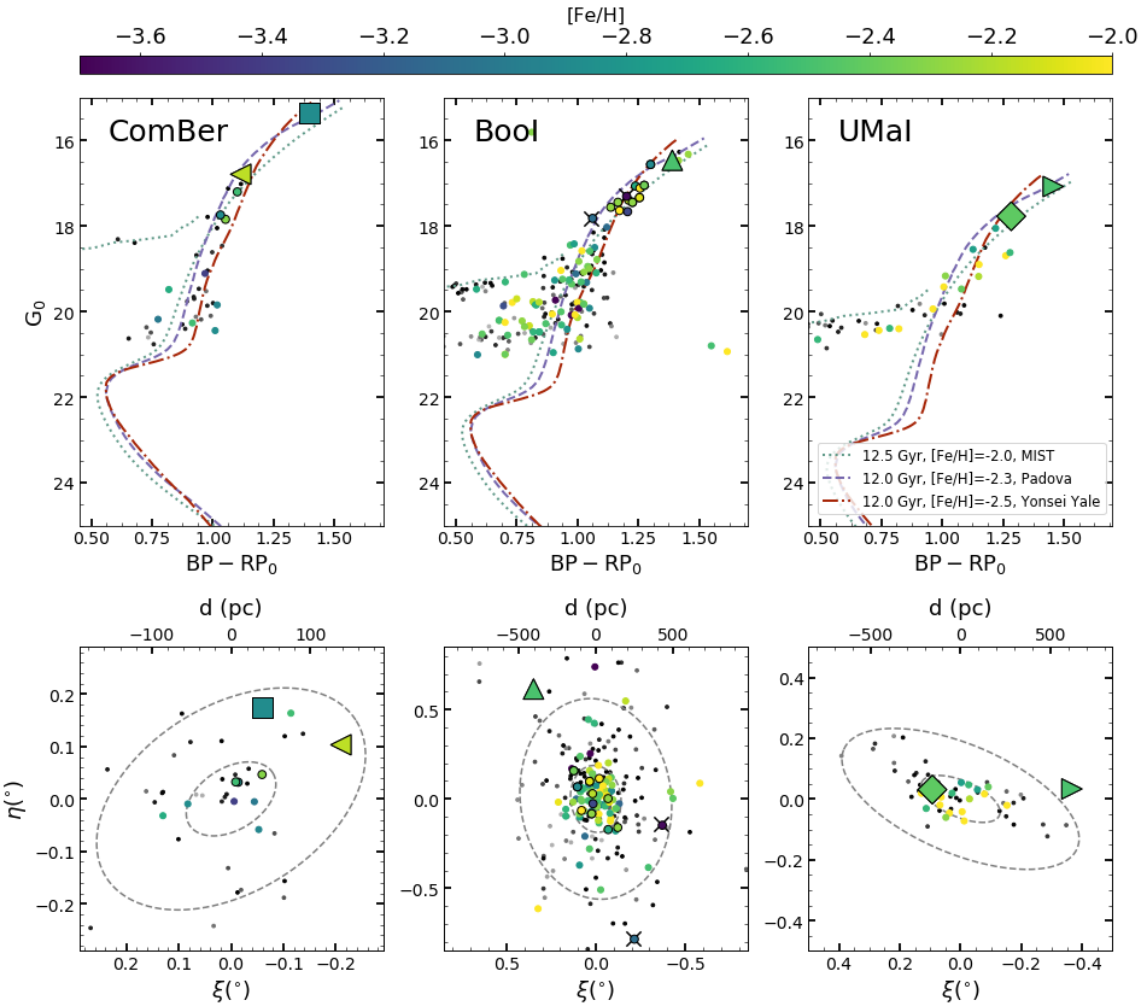

Figure 3.1: Top row: Gaia colour-magnitude diagram positions of our targets (large symbols) and those in the literature in three UFDs (see Appendix) coloured by their metallicities. Distances and reddening values used are Table 3.1. See text for information on the sample isochrones. Bottom row: On-sky positions in projected coordinates of stars in these UFDs with spectroscopic metallicities. Dashed lines at 1 and 3 R_h. Galactic ellipticities, position angles, and half-light radii are listed in Table 3.2. Large coloured symbols are our targets, medium-sized symbols with black outlines are those with high resolution spectroscopy in the literature, and small coloured symbols are those with low resolution metallicities (CaT, Mgb; see Appendix). In Boo I, additional stars with HRS analyses at > 2 R_h are marked with a black "X" (they are members). Targets from Gaia EDR3 with a high likelihood for membership are shown as small dark symbols, grey-scaled weighted by their P_{sat} values from McConnachie & Venn (2020b). Full list of literature targets is available online.

Table 3.1: Gaia EDR3 data for each target, as well as our GRACES observational details and their locations in each UFD. In the absence of consistent naming conventions for UFD stars, we use the following naming scheme in this paper, and include Gaia source IDs for cross-matching purposes.

Name	RA J2000 (hh mm ss)	Dec J2000 (dd mm ss)	G (mag)	BP−RP (mag)	Gaia sourceID
CB-1	12 26 43.5	24 04 45.7	15.40	1.42	3959888486031303424
CB-2	12 26 03.9	24 00 26.1	16.85	1.14	3959884740819808256
BooI-2	14 01 32.6	15 06 50.7	16.52	1.41	1231264907837100800
UMaI-1	10 32 30.1	51 57 04.9	17.12	1.48	847716356845689216
UMaI-2	10 35 28.9	51 57 01.5	17.82	1.31	849020961751785472

Name	Obs Date	t_{exp} (sec)	N_{exp}	SNR (5200, 6000)	loc. (R_h)	A_V
CB-1	2021-01-07	900	3	20, 35	2.5	0.054
CB-2	2021-01-07	1800	2	10, 16	2.5	0.061
BooI-2	2021-05-08	2400	4	15, 30	4.0	0.058
UMaI-1	2021-01-08	1800	3	7, 15	3.7	0.049
UMaI-2	2021-01-08	2400	4	7, 15	0.7	0.052

3.2 Target Selection

Targets were selected using an updated version of a new Bayesian inference method for finding highly probable members in UFDs, particularly in extended structures (Jensen et al., 2024; McConnachie & Venn, 2020b). This method uses Gaia photometry and astrometry (Gaia Collaboration et al., 2016b, 2021; Riello et al., 2021; Lindegren et al., 2021) to assign likelihoods for a star to be a member of one of the UFD galaxies, or of the Milky Way foreground. This was done based on their projected spatial positions and position in color-magnitude space. The models for these likelihoods are based on the derived structural parameters for each dwarf galaxy (including their uncertainties) and the known stellar populations of the dwarfs (including distance uncertainties). Importantly, radial velocity information is not used when assigning probabilities for individual stars.

A total of ten new targets were found in these three UFDs with membership likelihoods greater than 0.8; six stars in Com Ber, three stars in UMa I, and one in Boo I. We focus primarily on stars with separations $>2R_h$ from their galaxy's centers. In this paper, we present high-resolution spectroscopic (HRS) observations for five bright stars in northern UFDs, Com Ber, UMa I, and Boo I. Our method found

membership likelihoods > 0.999 for all five stars. Their distances range from central locations to $\sim 4R_h$ (see Table 3.1), where the R_h values for each UFD and other structural parameters are in Table 3.2.

This is the first model atmospheres analysis of stars in UMa I and nearly doubles the number of HRS analyses of stars in Com Ber. We included one star in Boo I because of its location (>3 R_h). In the absence of consistent naming conventions for UFD stars, we use the naming scheme given in Table 3.1 in this paper, and include Gaia source IDs for cross-matching purposes. The target positions and Gaia colours are listed in Table 3.1 and plotted on the colour-magnitude diagram in Fig. 3.1. Reddening values are from Schlegel et al. (1998). Sample isochrones are also shown in Fig. 3.1, where the MIST[1] isochrone including the horizontal branch is from Paxton et al. (2011), Choi et al. (2016), and Dotter (2016), and the Padova[2] isochrone is from Bressan et al. (2012). The Yonsei-Yale[3] isochrone is from Lejeune et al. (1998) and Demarque et al. (2004), where colours were converted to Gaia photometric bands using the Gaia DR2 Release Documentation (V1.2, 5.3.7).

Target locations and metallicities are shown in Fig. 3.1 along with metallicities from the literature. For Com Ber, these metallicities include medium resolution spectroscopy (MRS, R∼6000) from Vargas et al. (2013) and high resolution spectroscopy (HRS, R>30,000) from Frebel et al. (2010a). For UMa I, only MRS is available (from Martin et al., 2007; Vargas et al., 2013). One highly probable member was also found on the outskirts of the southern UFD, Boo I. The metallicities in Fig. 3.1 for stars in Boo I are from both LRS (Kleyna et al., 2005; Martin et al., 2007; Norris et al., 2010b; Lai et al., 2011; Jenkins et al., 2021) and HRS (Gilmore et al., 2013; Ishigaki et al., 2014; Feltzing et al., 2009; Frebel et al., 2016).

3.3 GRACES Observations and Reduction

High-resolution spectra have been collected using the Gemini Remote Access to CFHT ESPaDOnS Spectrograph (GRACES, Chene et al., 2014; Pazder et al., 2014). In the 2-fibre (object+sky) mode, spectra are obtained with resolution R∼65,000; however, light below ∼4800 Å is severely limited by poor transmission through the optical fibre

[1]MIST/MESA isochrones: http://waps.cfa.harvard.edu/MIST/
[2]Padova isochrones: http://stev.oapd.inaf.it/cmd
[3]Yonsei-Yale isochrones: http://www.astro.yale.edu/demarque/yyiso.html
[4]Available at: http://www.astro.uvic.ca/~alan/Nearby_Dwarf_Database_files/NearbyGalaxies_Jan2021_PUBLIC.fits

Table 3.2: Galactic parameters for our three UFD galaxies from McConnachie (2012, updated 2021[4]) RV is the range in radial velocities, $D_\odot$ is the heliocentric distance, *ell* and ϕ are the ellipticity and position angle of the isophotes, and R_h is the half light radius, for each UFD.

Name	RV range ($km\,s^{-1}$)	$D_\odot$ (kpc)	ell	ϕ (deg)	R_h (arcmin)	R_h (pc)
Com Ber	97.2 to 99.0	40 ±4	0.37	−58	5.63	65
UMa I	−56.7 to −53.9	97 ±4	0.57	67	8.34	235
Boo I	96.9 to 101.1	66 ±2	0.25	7	11.26	217

Table 3.3: The stellar parameters, effective temperature (T_{eff}) and surface gravity ($\log g$) for our MARCS model atmospheres. Metallicities ($[Fe/H]_{LTE}$) are from our spectral line analysis (see Section 3.5), and microturbulence (ξ) is calculated from Mashonkina et al. (2017). Values of $\log g$<0.5 were set to 0.5 to avoid extrapolating outside the MARCS grid. Radial velocities (RV) are found with IRAF/*fxcor* from our spectra. Parameters for HD122563 are from Mashonkina et al. (2017) and Karovicova et al. (2020).

Name	T_{eff} (K)	$\log g$ (dex)	ξ ($km\,s^{-1}$)	$[Fe/H]_{LTE}$ (dex)	RV ($km\,s^{-1}$)
CB-1	4385 ±81	0.33 ±0.12	2.1±0.1	−2.88±0.15	91.76 ±0.18
CB-2	4879 ±99	1.24 ±0.12	2.5±0.1	−2.16±0.12	95.86 ±0.27
BooI-2	4390 ±70	0.41 ±0.08	2.3±0.1	−2.49±0.14	99.25 ±1.09
UMaI-1	4308 ±68	0.28 ±0.12	2.1±0.1	−2.50±0.12	−51.73 ±0.38
UMaI-2	4574 ±83	0.75 ±0.11	2.4±0.1	−2.42±0.20	−53.78 ±0.98
HD122563	4635 ±34	1.40 ±0.04	1.7	−2.75±0.12	—

link.

The GRACES spectra have been reduced using the Gemini "Open-source Pipeline for ESPaDOnS Reduction and Analysis" tool (OPERA, Martioli et al., 2012), as described in Kielty et al. (2021). Briefly, this includes standard calibrations (including wavelength calibration and heliocentric corrections). Starting from the individually extracted and normalized échelle orders, one continuous spectrum is created by weighting the overlapping wavelength regions by their error spectrum, and co-adding as a weighted average. No radial velocity variations were found between the multiple visits ($\Delta RV \leq 1\,km\,s^{-1}$) for each star, and all visits per star have then been co-added via a weighted mean using the error spectrum. Each co-added spectrum was radial velocity corrected by comparisons with the metal-poor benchmark star HD 122563,

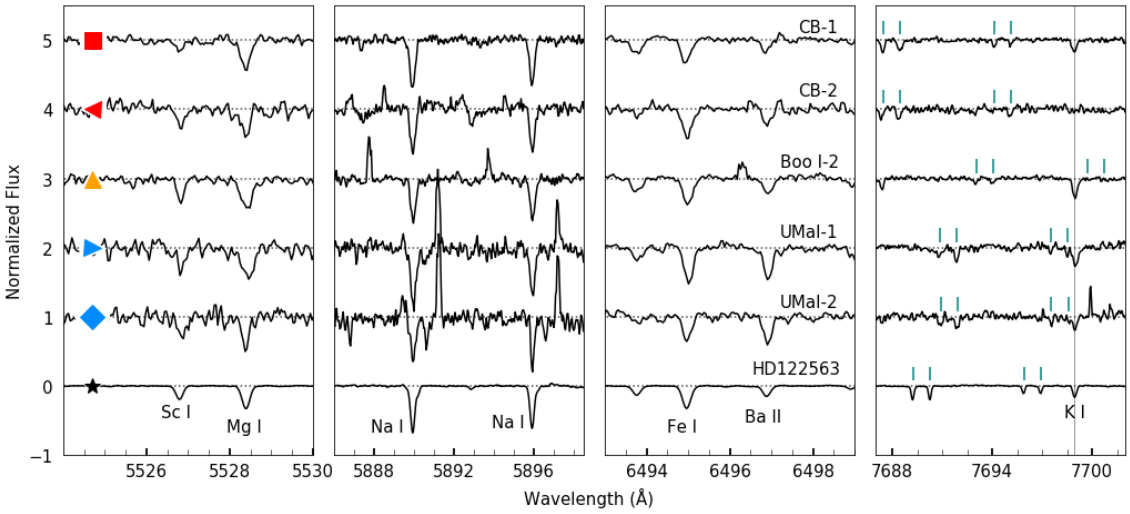

Figure 3.2: Samples of the GRACES spectra for five stars in three UFD galaxies, and the standard star HD122563. Coloured markers are the same as in Fig. 3.1. The improved SNR at redder wavelengths that is typical of GRACES spectra can clearly be seen in all cases. Key absorption features are marked for clarity. Equally-spaced absorption features from earth's atmosphere are marked in the right hand panel with blue dashes.

and re-normalized using asymmetric k sigma-clipping. This normalization routine can occasionally under-estimate the continuum due to small absorption lines being hidden in the noise. This is discussed in Section 3.5. Sample spectra are shown in Fig. 3.2.

3.4 Stellar Parameters

All five stars in this paper are expected to be red giants based on their magnitudes and membership in each UFD, as shown in Fig 3.1. This affects how stellar parameters are determined, which is described below. Our final stellar parameters per star are listed in Table 3.3.

Effective temperatures ($T_{\rm eff}$) have been determined using the colour-temperature relation for Gaia photometry from Mucciarelli & Bellazzini (2020, hereafter MB2020). This calibration was selected based on their inclusion of very metal-poor stars (from González Hernández & Bonifacio 2009). When calculating temperatures from MB2020, it is necessary to know if the star is a dwarf or giant (two sets of calibrations) and to have a metallicity estimate a priori. We adopted [Fe/H]$=-2.5$ for all stars, repre-

sentative of the metallicity estimates of these UFDs in the literature. We adopted an uncertainty of Δ[Fe/H]=$\pm$0.5 to propagate into our stellar parameter error estimates. A comparison of the temperatures from the MB2020 calibration to those from the colour-temperature relationship by Casagrande (2020) showed very good agreement in metal-poor halo stars (e.g., Kielty et al., 2021).

Surface gravities (log g) were determined using the Stefan-Boltzmann equation (e.g., Venn et al. 2017; Kraft & Ivans 2003). This method requires (i) a distance, which we took from the dwarf galaxy table in McConnachie (2012, updated 2021[4]), (ii) the solar bolometric magnitude of M_{bol} = 4.74, and (iii) bolometric corrections for Gaia DR2 photometry (Andrae et al., 2018). Any gravities with $\log g < 0.5$ were rounded up to 0.5 to keep them within the model atmosphere grid.

The metallicities listed in Table 3.3 are the final metallicities from our spectral lines analysis described below (see Section 3.5). Microturbulence is not needed for our stellar parameter determinations; however, we have included it in Table 3.3 for completeness as it is required for our model atmospheres analysis in Section 3.5. Microturbulence (ξ) was adopted from the calibrations for metal-poor red giants by Mashonkina et al. (2017).

3.4.1 Stellar Parameters: Uncertainties

Uncertainties in T_{eff} and $\log g$ were determined from a Monte Carlo analysis on the uncertainties from the input parameters, as well as assuming a flat prior on the stellar mass, spanning 0.5 to 1.0 $M_{\odot}$. The stellar parameters used in generating model atmospheres, T_{eff} and $\log g$, and their uncertainties, are listed in Table 3.3.

Uncertainties in metallicity are from our iron spectral line analyses (below). Meanwhile, the uncertainties in the microturbulence (ξ) values are initially taken from the calibration by Mashonkina et al. (2017). For weak lines in our spectral analysis (EW $<$ 150 mÅ), the uncertainties in ξ have very small to negligible impact on the stellar abundances. However, for a few elements (Mg, Na), we have been forced to keep stronger lines (up to 300 mÅ) since only one or no other spectral lines are available. Stronger lines are much more sensitive to ξ, however in all cases, we find the chemical abundance uncertainties are dominated by the uncertainties in T_{eff} and $\log g$, rather than ξ; see Section 3.5.3.

A spectroscopic method of finding the stellar parameters was also explored for one star (CB-1) with the most lines, by altering the T_{eff} to minimize correlation

between abundance and excitation potential, and by altering $\log g$ to produce similar abundances for first and second iron excitation states. The best fit $T_{\rm eff}$ and $\log g$ were found to be within 1σ of the parameters found through the MB2020 methods, confirming the quality of our method for determining the stellar parameters.

3.5 Spectral Lines Analysis

Radial velocities and chemical abundances are determined for each star from individual spectral lines. Spectral lines were selected from the recent GRACES analysis of metal-poor halo stars by Kielty et al. (2021), see Table 3.4. Radial velocities were determined using IRAF/*fxcor*. Each final combined spectrum was cross-correlated with a GRACES spectrum of the standard star HD 122563 (from Kielty et al. 2021) in the spectral region from 4800 to 6700 Å. The RV precision was dependent on the SNR of the spectra and stellar parameters of each star.

Chemical abundances were determined using the stellar parameters discussed above for a classical model atmospheres analysis. These stellar parameters were used to generate spherical model atmospheres with the (most up-to-date) models on the MARCS website (Gustafsson et al., 2008). The OSMARCS spherical models were used given that all the stars have $\log g < 3.5$. Atomic data was adopted from the *linemake*[5] atomic and molecular line database (Placco et al., 2021). Isotopic and hyperfine structure corrections were included for lines of Ba II.

Chemical abundances are compared to the Sun using standard notation $[{\rm X/Y}] = \log {\rm n(X)/n(Y)}_{*} - \log {\rm n(X)/n(Y)}_{\odot}$, where n(X) and n(Y) are column densities (in $\rm cm^{-2}$). We adopt the solar abundances from Asplund et al. (2009).

Two methods were explored in our chemical abundance analysis: (i) spectral line syntheses, and (ii) line-by-line equivalent width (EW) results. We found that an iterative process between the spectrum syntheses and the EW analysis per line yielded the most reliable results as the signal-to-noise (SNR) of our final combined 1D spectra was typically quite low. Each of these methods are discussed in the following two subsections.

[5] Available at https://github.com/vmplacco/linemake

Table 3.4: Sample line list, equivalent width (EW) measurements, and chemical abundances (where X = 12+log(X/H)) from both the EW (X_{EW}) and spectrum synthesis (X_{SYN}) analyses. Flags are as follows: "n" too noisy, "w" too weak, "b" a blend, "s" too strong (EW> 150 mÅ). Results in italics are strong lines which were used when no other lines are available. SNR values provided at 5200 A per star. χ is the excitation potential in eV, gf is log(gf). Full line list for all five stars available online.

				CB-1 (SNR=20)			CB-2 (SNR=10)			...
Wave.	Elem	χ	gf	EW	X_{EW}	X_{SYN}	EW	X_{EW}	X_{SYN}	
5216.274	26	1.607	-2.080	125	4.98	4.75	s	—	—	...
5232.940	26	2.938	-0.190	105	4.69	4.65	140	5.52	5.05	...
5247.050	26	0.087	-4.970	45	4.48	4.8	n	—	—	...
5250.210	26	0.121	-4.900	80	4.91	4.7	n	—	—	...
...										

3.5.1 Spectrum Syntheses

The 1D LTE radiative transfer code MOOG[6] (Sneden, 1973; Sobeck et al., 2011) was used to synthesize the stellar spectra using the stellar parameters as described above. This method was carried out in three steps: (1) a model atmosphere was generated with the initial parameters: T_{eff}, $\log g$ and ξ as described in Section 3.4, and an initial metallicity of -2.0. The iron lines were synthesized for a preliminary metallicity estimate, and the model atmosphere updated with the new metallicity. This process was repeated until the metallicity output matched the input (typically only twice). (2) A new synthesis of all elements was generated which included line abundances and upper limits for all of the clean spectral lines. (3) Hyperfine structure corrections were applied to barium from a full spectrum synthesis within ±10 Å of the Ba II lines.

Each synthetic spectra was broadened in MOOG to match the observed spectra; we found that a Gaussian smoothing kernel with FWHM=0.2 was a good match to the GRACES spectral resolution (which dominates the broadening for these low gravity red giant stars). If a spectral feature was well fit, then we calculated an abundance for that line. If not, then a 3σ upper limit was calculated. Amongst the upper limits that were calculated, none other than one K I line provided a useful scientific constraint.

Additional spectral lines were sought once we had preliminary results for each of the five targets in this paper. Any new spectral features found and measured

[6] Available at http://www.as.utexas.edu/~chris/moog.html

were collated into our master line list (see Table 3.4), which was then used for a full synthesis of each stellar spectrum. The full and final synthesis was carried out with the final stellar and spectral parameters and compared to the equivalent widths method as described below.

3.5.2 Equivalent Widths Analysis

Equivalent widths (EW) were measured in IRAF/*splot* (Tody, 1986, 1993) and provided in Table 3.4. Weak lines were measured by fitting a Gaussian profile, and stronger lines were examined by also integrating under the continuum or where noise made fitting impossible. The continuum was carefully examined, and adjustments upwards by $\leq$10% was occasionally necessary to account for weak lines in the low SNR spectra.

Abundances were determined by assuming local thermodynamic equilibrium (LTE) and examining the EW line measurements in MOOG. The microturbulence (ξ in $\mathrm{km\,s^{-1}}$) was examined and slightly adjusted to minimize any EW-abundance correlations in the Fe I lines. Lines with abundances well above or below the 1σ line scatter were confirmed to be blends or noise spikes respectively, and discarded. Comparison of the equivalent width and the syntheses methods allowed us to remove or flag line-confounding noise spikes (e.g. a noise spike in the middle of the trough). Iron lines with EW >150 mÅ were flagged as strong and discarded.

Correlations between the Fe I line abundances with excitation potential, equivalent width, and wavelength were confirmed to be minimal before proceeding. This was to check the stellar parameters and data reductions. Ionization balance between Fe I and Fe II was also examined as a check on the surface gravities (including NLTE corrections; see below). For three stars (CB-1, UMaI-1, and BooI-2), we were forced to adopt a slightly larger surface gravity ($\log g$=0.5) which would also have a small effect on the Fe I and Fe II abundances.

The final calculations included all updates from these tests (line lists, metallicities and microturbulence). As a final step, hyperfine-structure corrections were applied to the Ba II analyses.

Table 3.5: Sample uncertainties for the CB-1 and UMaI-1 analyses (the two stars with the highest and lowest SNR, respectively). Systematic errors in the abundances due to the uncertainties in the stellar parameters, T_{eff}, $\log g$, metallicity and microturbulence from Table 3.3 are listed as ΔT, Δg, Δm, and $\Delta \xi$. The line scatter for the equivalent widths and syntheses methods from Table 3.4 are denoted as σ_{EW} and σ_{syn}. All values have the same units as the solar scaled log abundance denoted by [X/H]. For species with fewer than 5 lines, the scatter from Fe I was adopted, reduced by $\sqrt{n}$ of the species. ΔEW and Δsyn are the full errors per element species from the line scatter and the stellar parameter abundance errors, added in quadrature. Full table for the other four stars in the Appendix.

species	ΔT	Δg	Δm	$\Delta \xi$	σ_{EW}	σ_{syn}	ΔEW	Δsyn
CB-1								
Fe I	0.14	0.00	0.04	0.01	0.02	0.05	0.15	0.15
Fe II	0.04	0.02	0.01	0.01	0.10	0.14	0.11	0.15
Na I	0.18	0.01	0.06	0.03	0.14	0.17	0.24	0.26
Mg I	0.10	0.04	0.03	0.02	0.11	0.13	0.16	0.17
K I	0.11	0.01	0.03	0.01	0.20	—	0.23	—
Ca I	0.08	0.02	0.04	0.01	0.03	0.08	0.10	0.12
Sc I	0.12	0.01	0.02	0.02	—	0.20	—	0.24
Ti I	0.19	0.00	0.06	0.01	0.08	0.09	0.21	0.22
Ti II	0.00	0.03	0.01	0.01	0.09	0.09	0.09	0.10
Cr I	0.16	0.00	0.06	0.02	0.11	0.09	0.21	0.19
Ni I	0.14	0.00	0.04	0.01	0.14	0.12	0.20	0.19
Ba II	0.05	0.04	0.02	0.01	0.14	0.13	0.15	0.14

Table 3.6: Sample of the NLTE corrections (Δ_{NLTE}) from two databases, INSPECT and MPIA (see text), such that $X_{NLTE} = X_{LTE} + \Delta_{NLTE}$. Full table of NLTE corrections for all five stars is available online. K and Ba corrections are from Andrievsky et al. (2010) and Mashonkina & Belyaev (2019) respectively, and marked in the Inspect column with a * in the full table.

		CB-1		CB-2		UMaI-1		...
Wave.	Elem	Inspect	MPIA	Inspect	MPIA	Inspect	MPIA	...
5216.274	26.0	0.147	0.205	—	—	—	—	...
5232.940	26.0	0.074	0.236	0.062	0.057	—	—	...
5247.050	26.0	0.130	0.198	—	—	0.159	0.138	...
5250.210	26.0	0.145	0.094	—	—	0.152	0.064	...
...								

Table 3.7: Scaled-solar chemical abundances from our EW analyses, except for species labelled with an * which are from syntheses, with and without NLTE corrections (in Table 3.6). Metallicity [Fe/H] is a weighted mean of [Fe I/H] and [Fe II/H]. Solar abundances as 12+log(X/H) from Asplund et al. (2009), and $[X/Fe] = \log(X/Fe)_* - \log(X/Fe)_\odot$. Species such as Ni I which have no available NLTE corrections still show an altered value in the NLTE table, which is strictly due to the Fe NLTE corrections. Numbers in parentheses indicate the number of lines contributing to the mean.

LTE

	Solar	CB-1	CB-2	UMaI-1	UMaI-2	BooI-2
	log(X/H)	[X/Fe]	[X/Fe]	[X/Fe]	[X/Fe]	[X/Fe]
[Fe/H]	7.50	-2.88±0.15 (77)	-2.17±0.12 (46)	-2.49±0.12 (44)	-2.42±0.20 (45)	-2.49±0.14 (61)
[Fe I/H]	7.50	-2.88±0.15 (73)	-2.15±0.12 (41)	-2.51±0.12 (42)	-2.42±0.20 (43)	-2.49±0.14 (55)
[Fe II/H]	7.50	-2.97±0.11 (4)	-2.32±0.11 (5)	-2.04±0.15 (2)	-2.46±0.17 (2)	-2.45±0.10 (6)
[Na I/Fe]	6.24	0.30±0.24 (2)	-0.13±0.22 (2)	-0.30±0.20 (2)	-0.73±0.29 (2)	-0.63±0.22 (2)
[Mg I/Fe]	7.60	0.87±0.16 (3)	0.02±0.17 (3)	0.19±0.14 (3)	0.44±0.23 (1)	0.69±0.23 (1)
[K I/Fe]	5.03	0.65±0.23 (1)	<0.28±0.23 (1)	0.55±0.24 (1)	0.26±0.23 (1)	0.64±0.24 (1)
[Ca I/Fe]	6.34	0.74±0.10 (13)	-0.21±0.12 (5)	0.09±0.14 (11)	0.32±0.16 (6)	0.22±0.11 (12)
[Sc I/Fe]*	3.13	-0.10±0.24 (1)	0.00±0.22 (1)	0.70±0.24 (1)	0.00±0.24 (1)	0.10±0.24 (1)
[Ti I/Fe]	4.95	0.22±0.21 (7)	0.25±0.16 (5)	0.42±0.24 (2)	— (0)	0.40±0.21 (4)
[Ti II/Fe]	4.95	0.38±0.09 (4)	— (0)	0.90±0.12 (3)	— (0)	0.20±0.15 (2)
[Cr I/Fe]	5.64	-0.18±0.21 (3)	0.01±0.18 (3)	-0.56±0.21 (2)	0.03±0.27 (2)	-0.58±0.21 (2)
[Ni I/Fe]	6.22	-0.13±0.20 (2)	0.53±0.16 (5)	0.07±0.14 (4)	-0.01±0.27 (2)	-0.12±0.16 (5)
[Ba II/Fe]	2.18	-1.10±0.15 (2)	-0.95±0.18 (2)	-0.39±0.12 (3)	-0.43±0.17 (3)	-1.20±0.16 (2)

cont. next page...

NLTE

	Solar	CB-1	CB-2	UMaI-1	UMaI-2	BooI-2
	log(X/H)	[X/Fe]	[X/Fe]	[X/Fe]	[X/Fe]	[X/Fe]
[Fe/H]	7.50	-2.69±0.15 (77)	-2.02±0.12 (46)	-2.37±0.12 (44)	-2.27±0.20 (45)	-2.35±0.14 (61)
[Fe I/H]	7.50	-2.68±0.15 (73)	-1.99±0.12 (41)	-2.39±0.12 (42)	-2.26±0.20 (43)	-2.34±0.14 (55)
[Fe II/H]	7.50	-2.88±0.11 (4)	-2.28±0.11 (5)	-2.04±0.15 (2)	-2.38±0.17 (2)	-2.40±0.10 (6)
[Na I/Fe]	6.24	-0.17±0.24 (2)	-0.75±0.22 (2)	-0.53±0.20 (2)	-1.12±0.29 (2)	-0.97±0.22 (2)
[Mg I/Fe]	7.60	0.76±0.16 (3)	-0.07±0.17 (3)	0.12±0.14 (3)	0.35±0.23 (1)	0.61±0.23 (1)
[K I/Fe]	5.03	0.19±0.23 (1)	<-0.20±0.23 (1)	0.23±0.24 (1)	-0.1±0.23 (1)	0.29±0.24 (1)
[Ca I/Fe]	6.34	0.74±0.10 (13)	-0.21±0.12 (5)	0.10±0.14 (11)	0.37±0.16 (6)	0.24±0.11 (12)
[Sc I/Fe]*	3.13	-0.30±0.20 (1)	-0.20±0.20 (1)	0.50±0.20 (1)	-0.20±0.20 (1)	-0.10±0.20 (1)
[Ti I/Fe]	4.95	0.50±0.21 (7)	0.57±0.17 (5)	0.77±0.25 (2)	— (0)	0.66±0.21 (4)
[Ti II/Fe]	4.95	0.27±0.09 (4)	— (0)	0.73±0.12 (3)	— (0)	0.13±0.15 (2)
[Cr I/Fe]	5.64	0.08±0.21 (3)	0.23±0.18 (3)	-0.35±0.21 (2)	0.29±0.27 (2)	-0.33±0.21 (2)
[Ni I/Fe]	6.22	-0.32±0.20 (2)	0.38±0.16 (5)	-0.05±0.14 (4)	-0.16±0.27 (2)	-0.26±0.16 (5)
[Ba II/Fe]	2.18	-1.20±0.15 (2)	-1.06±0.18 (2)	-0.41±0.12 (3)	-0.53±0.17 (3)	-1.25±0.16 (2)

3.5.3 Measurement and Parameter Uncertainties

The measurement errors from both the synthesis and EW methods are from the line-to-line scatter in the abundances, $\sigma_{\rm syn}$ and $\sigma_{\rm EW}$, respectively (see Table 3.5). These represent errors in the continuum placement, local SNR, and atomic data quality. For elements with few lines (<5), the standard error from FeI was adopted and reduced by $\sqrt{n}$, where n is the number of lines available.

The chemical abundances are also subject to systematic errors from the uncertainties in our model parameters. For each program star, we varied $T_{\rm eff}$, $\log g$, [M/H], and ξ, one at a time, by the uncertainties given in Table 3.3. The corresponding abundance uncertainties are listed as δT, δg, δm, and $\delta \xi$.

Total abundance uncertainties, Δ_{syn} and Δ_{EW}, were calculated by adding in quadrature the line-to-line abundance scatter, with the uncertainties imposed by the stellar parameter errors. These are adopted in the abundance plots in Section 3.6.

3.5.4 NLTE corrections

Departures from Local Thermodynamic Equilibrium (LTE) due to the radiation field in metal-poor red giants are known to impact the statistical equilibrium solution for elements like Fe I. These non-LTE (NLTE) effects can be large, significantly affecting stellar abundance solutions (e.g., $\Delta\log(\rm X/H) > 0.2$). To investigate the impact of NLTE corrections on our iron abundances, and other elements, we examine three databases and a paper; the MPIA[7] for Fe I and Fe II (Bergemann et al., 2012), Mg I (Bergemann et al., 2017), Ca I (Mashonkina et al., 2017), Ti I and Ti II (Bergemann, 2011), and Cr I (Bergemann & Cescutti, 2010). We also examine the NLTE corrections available from the INSPECT[8] database for these corrections as listed in Table 3.6, and INSPECT also includes NLTE corrections for Na I (Lind et al., 2012). A comparison of the MPIA and INSPECT corrections for lines and elements in common suggests that the MPIA corrections are generally larger (more positive). The NLTE corrections per line are included in Table 3.6.

Finally, NLTE corrections for lines of Ba II are from calculations by Mashonkina & Belyaev (2019), also available online[9], and NLTE corrections for K I are taken from Andrievsky et al. (2010). These are included in Table 3.6. (The full table of NLTE corrections is currently in the Appendix).

[7]MPIA NLTE corrections: http://nlte.mpia.de.
[8]INSPECT NLTE corrections: http://inspect-stars.com.
[9]Mashonkina Ba II NLTE corrections: http://www.inasan.ru/~lima/pristine.

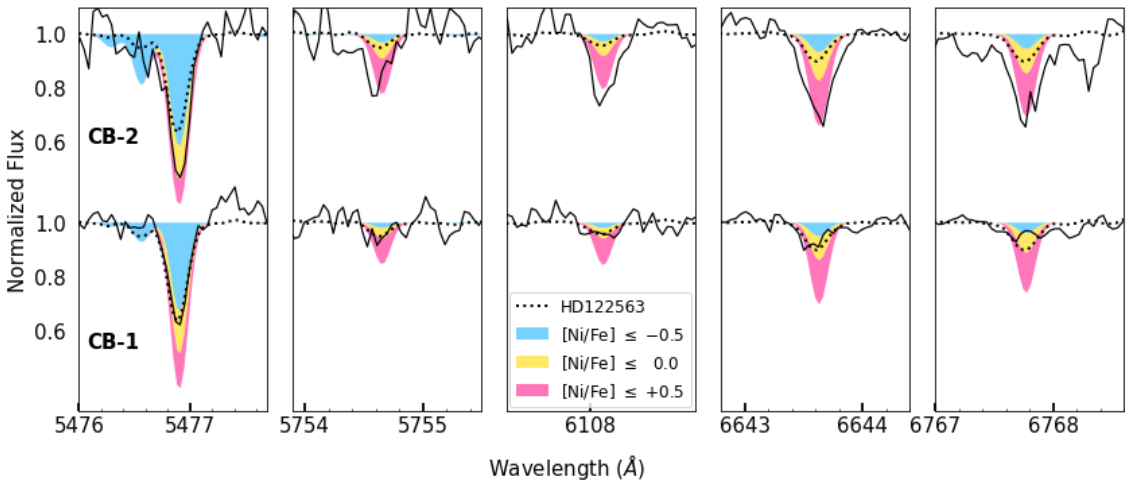

Figure 3.3: Ni I lines for the two stars in Com Ber compared to synthetic spectra with corresponding stellar parameters and the standard star HD 122563. We show Ni-rich (pink) and Ni-poor (blue) values to clarify the Ni-enrichment in the star CB-2.

3.6 Chemical Abundances

The chemical abundances for five stars in three UFDs were uniquely determined from both a spectrum synthesis (Section 3.5.1) and an EW analysis (Section 3.5.2). All abundances are reported in Table 3.7 and discussed in the context of their host galaxies in Section 3.7. The results from our EW and spectrum synthesis methods are in good agreement, and the process of iterating between the two methods provided an effective filter for unreliable lines due to the low SNR. Our method suggests that the EW abundances have slightly higher precision (but not necessarily accuracy), with the exception of Sc and Ba for which isotopic and hyperfine structure corrections are included in the syntheses. NLTE corrections are applied to all elements, and adopt in this paper.

3.6.1 Iron-Peak Elements

The iron-peak elements in very metal-poor stars are expected to have formed primarily in core collapse supernova (Tolstoy et al., 2009; Heger & Woosley, 2010). At higher metallicities, iron-peak elements are also formed in SN Ia, either through the single or double degenerate scenarios (Nomoto et al., 2013). In this paper, we examine iron, chromium, and nickel.

Iron is determined from $40-70$ Fe I lines and $2-6$ Fe II lines, and [Fe/H] is

the weighted average. We find the abundances of Fe I and Fe II are in excellent agreement ($\leq 1\sigma$) for all stars except UMa I-1. This star has a very low predicted gravity, $\log g$=0.3, which is slightly beyond the model atmosphere grid parameters. As such, we rounded $\log g$ up to 0.5 for our analysis. This small offset may affect our Fe II values slightly, but more importantly, we have poor constraints on Fe II from only 2 lines. Furthermore, the typical NLTE corrections for Fe I are $\sim +0.1 - 0.2$, and < 0.1 for Fe II, which also provides a small improvement in the iron ionization equilibrium for UMa I-1.

Chromium abundances are determined from 2−3 Cr I lines, with significant NLTE corrections that raise these values. We note that most analyses in the literature do not apply NLTE corrections, thus we examine both LTE and NLTE results (below).

Nickel is from $2 - 5$ Ni I lines, where none have published NLTE corrections. We find a surprisingly high [Ni/Fe] abundance in one star, CB-2. This can be seen directly in the spectra as well (see Fig. 3.3, and discussed further in Section 3.6) For all three stars in Fig. 3.3, the Ni I 5476 line produces a ~ 0.5 dex lower abundance than the other four lines. While we have kept this line in the average Ni I abundances, we suggest there is an unknown systematic error (e.g., neglected NLTE corrections).

3.6.2 Alpha Elements

Alpha elements are even-Z elements that form primarily from helium nuclei captures during the carbon-, neon- and silicon-burning phases of massive star evolution, and through the α-rich freeze-out during core collapse supernovae. Recently, it has also been recognized that the interstellar medium may be enriched in α-elements at early times through the winds of rapidly rotating massive stars (e.g., Limongi & Chieffi, 2018; Kobayashi et al., 2020b). In this paper, the α-elements are limited to magnesium, calcium, and titanium due to the low metallicity of our targets and the limited wavelength coverage of the GRACES spectrograph.

Magnesium abundances are determined from one weak line of Mg I near 5528Å, and the stronger Mg I b lines at 5172 and 5183Å (see Table 3.4). The stronger lines are particularly sensitive to small uncertainties in the model atmospheres. The NLTE corrections for all Mg I lines in this analysis are small (~ -0.1).

Calcium abundances are from 5−13 Ca I lines. The Ca II triplet lines near ∼8000Å were excluded because of their large EW and sizable NLTE corrections, despite being in a higher SNR wavelength region of our GRACES spectra. NLTE corrections are

small, and typically similar to the average of the Fe I lines, such that $[\mathrm{Ca/Fe}]_{\mathrm{NLTE}} \sim [\mathrm{Ca/Fe}]_{\mathrm{LTE}}$.

Titanium is determined from up to 7 (4) Ti I (Ti II) lines, although no Ti lines were measurable in UMa I-2. Both species of Ti have significant NLTE corrections, although in opposite directions.

3.6.3 Odd-Z Elements

Odd-Z elements are important indicators of core collapse supernova yields, as the difference in the energetic requirements for α particle capture versus neutron capture produces a noticeable odd-even effect in the predicted yields (Heger & Woosley, 2010; Takahashi et al., 2018). From our Gemini/GRACES spectra, we are able to observe a small handful of odd-Z element spectral lines, including sodium, potassium, and scandium (Na, K, and Sc).

Sodium abundances are from the two strong Na I D resonance lines near 5890 and 5895 Å. These are present in all five of our target stars, where the stellar components are easily separated from the interstellar components, due to the radial velocities of our targets. Not only are these lines strong, and therefore sensitive to small uncertainties in the model atmospheres, but they also suffer from significant NLTE effects as resonance lines. We find NLTE corrections up to $\Delta_{\mathrm{NLTE}} \sim -0.5$ dex (see Table 3.6). We retain these lines for our analysis as the only measureable lines of an odd-Z element (Na), and note their sensitivities to the model atmosphere parameters represented by their larger errorbars.

Potassium is measured from the K I 7699 Å resonance line. This region is significantly affected by telluric features (see Fig. 3.2); however, the line is clear and present in most of our targets and comparison star HD 122563. NLTE corrections are significant, ~ -0.4 dex, caused by an over-recombination on the first energy level of this spectral line in the atmospheres of late-type stars (Andrievsky et al., 2010).

Scandium is measured from the Sc I 5527 Å line in all of our targets, as clearly seen in Fig. 3.2. As an odd-Z element, it has significant hyperfine structure corrections, which are taken into account through the spectrum syntheses. NLTE corrections are small, ~ -0.2 dex, taken from Battistini & Bensby (2015) per star.

3.6.4 Neutron-capture Elements

Neutron-capture elements are primarily formed through rapid-neutron capture in core collapse supernovae and neutron-star mergers, and slow-neutron capture during thermal-pulsing in AGB stars. The ratio of [Ba/Fe] produced in core-collapse supernovae (CCSNe) is expected to provide an r-process Ba floor, with contributions from the other processes building above that. To ascertain these different nucleosynthetic sources, often it is necessary to observe a pure r-process element (usually Eu). Unfortunately, Eu has only a very weak line near 6645 Å in the GRACES spectra, which is too weak to measure at our SNR. The stronger Eu II line near 4129 Å is outside the wavelength range of GRACES.

Barium is determined from two Ba II lines near 6141 and 6496 Å. In the two UMaI stars, the weaker Ba II line near 5853 Å is visible due to the higher Ba abundances in these stars. We report the abundance from this line in Table 3.7, but we do not use this line in the average [Ba/Fe] values due to very low SNR and inconsistent results with the two higher SNR lines. This element requires corrections for hyperfine structure and isotopic splitting, taken into account in our analysis through spectrum syntheses. We used an isotopic mixture characteristic of the r-process which includes no contributions from ^{134,136}Ba (Arlandini et al., 1999; Sneden et al., 2008). NLTE corrections are also applied, determined from Mashonkina & Belyaev (2019).

3.7 Chemical History of Ultra-Faint Dwarfs

3.7.1 Membership in the UFD hosts

In this paper, we present high resolution spectroscopic analyses for five stars in three ultra faint dwarf galaxies; Com Ber, UMa I, and Boo I. This project was partially motivated as a test of our target selection methodology, described in McConnachie & Venn 2020b, and its application to targets well beyond the tidal radius of their host galaxy. The radial velocities and low metallicities of our targets suggest that each is associated with their host UFD galaxy, providing excellent validation of our Bayesian inference method for finding highly probable members in UFDs from Gaia photometry and astrometry, with or without *a priori* radial velocities or metallicity information.

In Fig. 3.4, the radial velocities (RVs) and metallicities ([Fe/H]) of our targets are shown relative to others in the literature as a function of half-light radius in each

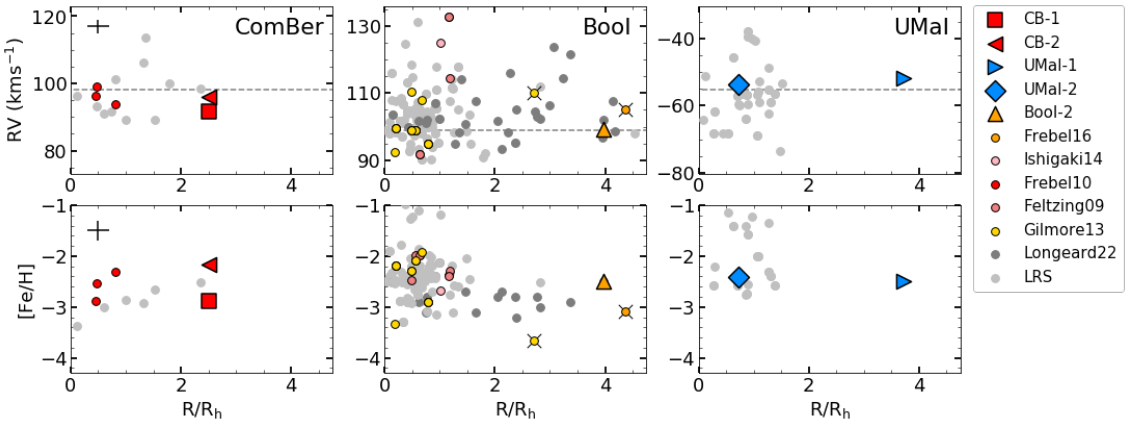

Figure 3.4: Radial distance in units of the half-light radius for all apparent members of our three ultra faint dwarf galaxies, compared with spectroscopically determined radial velocities (upper) and metallicities (lower; see online table for full list). Coloured points with black outlines are from HRS analyses. Low- and medium-res observations (LRS) are grey points. Dashed line shows the mean heliocentric radial velocity of the galaxy (see Table 3.2). Stars with HRS beyond $R \gtrsim 2R_h$, are additionally marked with a black "X" (they are members). Different observations of the the same star are *not* plotted twice, only the most recent data is shown. Sample uncertainty in R is from the uncertainty in galactic half-light radius from McConnachie (2012). Sample uncertainties of Δ[Fe/H] = 0.2 and ΔRV = 2 km s^{-1}are shown in the left panels only.

UFD. Light grey dots show results from LRS (Kleyna et al., 2005; Muñoz et al., 2006; Martin et al., 2007; Simon & Geha, 2007; Norris et al., 2010b; Koposov et al., 2011; Lai et al., 2011; Vargas et al., 2013; Jenkins et al., 2021; Longeard et al., 2022) and coloured dots are HRS from Frebel et al. (2010a); Feltzing et al. (2009); Gilmore et al. (2013); Ishigaki et al. (2014); Frebel et al. (2016). Our metallicities are consistent with stars located in the central regions. A similar result was seen in Boo I by Longeard et al. (2022), who selected targets[10] for MRS from the Pristine survey (Starkenburg et al., 2017b). The positions of the members in Fig. 3.1 do not suggest that Com Ber or Boo I are surrounded by elongated streams; however, the distribution of stars along the major-axis of UMa I is quite interesting. This was also noticed by Simon (2019), and is strengthened by our analysis of the outermost member (UMa I-1).

For comparison, Chiti et al. (2021) interpret the presence of one member of the

[10]We note that nearly all of the targets selected by Longeard et al. (2022) have P$_{sat}$ > 0.75 when using our selection criteria, which did not include metallicity. Two of their other outermost stars have P$_{sat}$ ∼ 0.6, and only their most distant and metal-poor star ([Fe/H]∼ −4 at ∼ 4 R$_h$) had P$_{sat}$ ∼ 0.2.

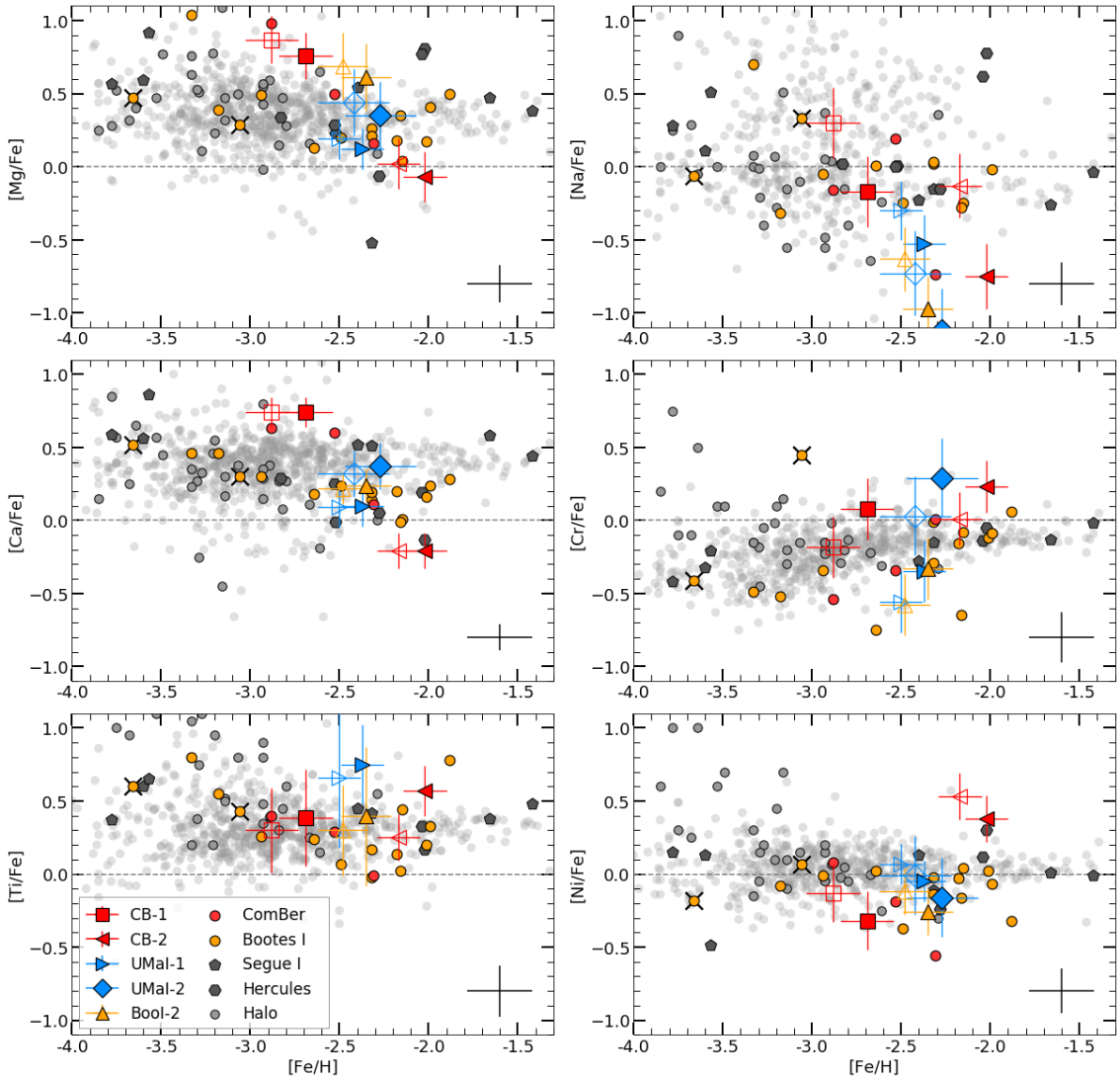

Figure 3.5: Markers with dark outline indicate hi-res observations, except for halo stars, for which it indicates the same analysis tools used as in this paper. Stars with model atmospheres analyses at $\gtrsim 3$ R_h, Boo-980 ([Fe/H]$= -3.1$), and Boo-1137 ([Fe/H]$= -3.7$), are additionally marked with a black x. For our data, filled: NLTE, and unfilled: LTE. Most reference data is LTE. Ti values were averaged over Ti I and Ti II, and large differences between the two are shown in the large error bars. α-element abundances drop to solar at [Fe/H] -2.2, with new observations in Mg and Ca consistent. (Halo: Yong et al. 2013, 2021; Aoki et al. 2013; Roederer et al. 2014, Halo marked with black outlines Kielty et al. 2021; Com Ber: Frebel et al. 2010a; Boo I: Norris et al. 2010a; Ishigaki et al. 2014; Gilmore et al. 2013; Frebel et al. 2016 ; Hercules: Koch et al. 2008, 2013; François et al. 2016; Segue I: Frebel et al. 2014.

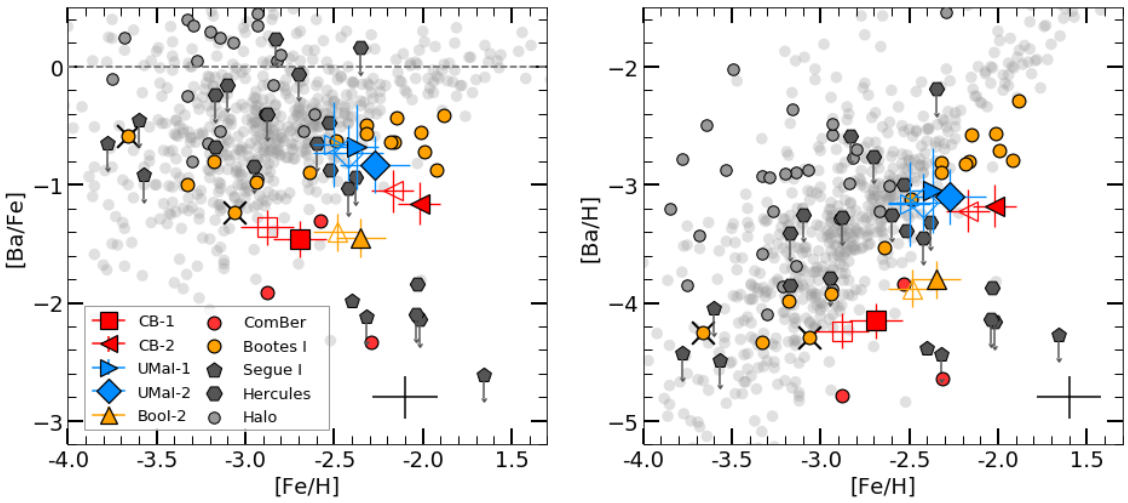

Figure 3.6: Exploration of the barium abundances in three UFD galaxies. Some stars can be seen at the r-process floor, [Ba/H] $\lesssim -4$. We suggest the barium abundances in Com Ber are due to inhomogenous mixing of (or lack of) SN Ia and AGB yields, and not the "one shot" model of yields from rare faint supernovae (see text). Symbols are the same as in Fig. 3.5.

UFD Tuc II at $\sim$9 R_h as evidence for either tidal stripping through interactions with the MW halo, strong bursty feedback during star formation that can provide a kick to the stellar dynamics, or possibly the remnant of an early dwarf galaxy minor merger. We suggest that deeper searches into the outskirts of the UFDs, now possible with the exquisite Gaia DR3 data, may provide new opportunities to study minor mergers in dwarf galaxies to recover the conditions in very low mass and pristine systems from the earliest epochs.

3.7.2 Chemical Abundances in the UFDs

High-resolution hydrodynamic simulations of UFD galaxies suggest that the baryonic component of these dark matter dominated systems are characterized by bursty star formation histories, truncated early by reionization. The stars formed during these bursts will be strongly clustered in location and chemically similar (Wheeler et al., 2019; Revaz & Jablonka, 2018; Applebaum et al., 2021). Deep color-magnitude diagrams provide observations that identify the stellar populations observed in the UFDs as old (>10 Gyr) and very metal-poor ([Fe/H]< -2; McConnachie 2012; Weisz et al. 2014; Brown et al. 2014; Laevens et al. 2015). Thus, UFDs have been proposed as fossils from the epoch of reionization, having undergone very little evolution since

that time.

The simulations further predict that the stars we observe today (z=0) in the UFDs may include the chemical signatures of Population III stars and the earliest supernovae (Tumlinson, 2010; Frebel & Bromm, 2012; Hartwig et al., 2018; Ishigaki et al., 2018). It may be possible to use detailed abundance patterns to constrain the mass of the first stars to pollute these systems. For example, very massive pair-instability supernovae (PISNe) predict stars with unusually deficient neutron-capture element yields (e.g., Ba) and high ratios of [Ca/Mg] (Takahashi et al., 2018), along with the classic odd-even effect (Heger & Woosley, 2010). Alternatively, lower mass metal-poor events can produce "faint supernova", which underproduce both the iron-peak and heavier elements, as well as the brightness of the supernova event, as ^{56}Ni falls into the core during collapse (Nomoto et al., 2013).

One challenge to UFD simulations has been the predicted metallicities of the lowest mass systems, and thereby the observed metallicity distributions, let alone the detailed chemical abundances. For example, Wheeler et al. (2019) were able to reproduce many observations of the lowest mass dwarf galaxies (mass, M/L ratio, size, frequency, star formation histories), however they were not able to reproduce the observed stellar metallicities. Simulated metallicities were too low, as gas is lost from low mass systems through supernova feedback. Multiple suggestions were offered, including pre-enrichment from Population III stars, pre-enrichment from a more massive host galaxy, and varying nucleosynthetic yields (Revaz & Jablonka, 2018; Wheeler et al., 2019), or that the feedback adopted was too efficient (Agertz et al., 2020). More recent zoom-in cosmological simulations of the UFDs by Applebaum et al. (2021) find better agreement between stellar metallicities and simulations when total metals (Z) is used, which includes all elements (dominated by oxygen rather than iron). Thus, a metallicity floor of log $(Z/Z_{\odot}) = -4$ is more successful at reproducing the observed metallicities in the UFDs than a floor of [Fe/H]$= -4$.

Some UFD simulations have sufficient numbers of stars to show a metallicity distribution. Nucleosynthetic events will enrich a local bubble of the interstellar gas, resulting in significant dispersions in the star-to-star metallicities and [X/Fe] ratios from stochastic sampling of the interstellar gas (e.g., Applebaum et al., 2021; Kobayashi et al., 2020b; Revaz & Jablonka, 2018; Fenner et al., 2006). However, metallicity distributions or *gradients* may also signal evidence for a dwarf galaxy halo, formed through minor merging of sub-halos (Benítez-Llambay et al., 2016; Deason et al., 2022). In the rest of this section, we discuss the chemical abundances of

the three UFDs in this paper in terms of their physical properties and evolutionary histories. All abundances are reported in Table 3.7 and shown in Figs. 3.5 and 3.6 compared to stars in the MW halo (Aoki et al., 2013; Yong et al., 2013, 2021; Roederer et al., 2014; Kielty et al., 2021). We also compare to stars in the UFDs Segue I (Frebel et al., 2014) and Hercules (Koch et al., 2008, 2013; François et al., 2016) because these two UFDs have stars with similar metallicities and chemical abundances to Com Ber.

3.7.2.a Com Ber

Com Ber is a UFD with total mass $M \approx 1.2 \times 10^6$ $M_\odot$ (Simon & Geha, 2007), apparent and absolute magnitudes of $m_V \approx 14.1$ and $M_V \approx$ -4.1, half-light radius $R_h \approx 65$ pc, and at a distance of $D \approx 40$ kpc (McConnachie, 2012). Simon (2018) suggests, based on Gaia DR2, that Com Ber is currently within 4 kpc of its pericenter. A study of the star-forming history of Com Ber using HST photometry suggests that most (>75%) of its stars may have formed before the epoch of reionization (Brown et al., 2014).

Three bright stars ($V < 18.1$) were analysed from high resolution spectroscopic data by Frebel et al. (2010a) who measured elemental abundances (C to Zn), and some neutron-capture elements (Sr to Eu). They found a significant metallicity dispersion from $-3 <$ [Fe/H] < -2, and an unusually low neutron-capture element ratios in two stars with [Fe/H]~ -2. It was unclear how such "high" iron abundances could have happened without contributions to the heavier elements. Similar abundance patterns were seen in other UFD galaxies, leading Frebel & Bromm (2012) to develop a set of stellar abundance signatures that could be the products of chemical "one-shot" events, where only one stellar generation forms after the first Population III SN explosions and yields are dominated by only one or a few massive core collapse supernovae. For Com Ber, it was proposed that a single, metal-free, ~20 $M_\odot$ faint supernova produced the abundance distribution observed (although faint supernova are expected to be very rare events; Kobayashi et al. 2020b). Furthermore, Sitnova et al. (2021) conducted a NLTE re-analysis of the three stars from Frebel et al. (2010a) and found amongst the lowest [Na/Fe] abundances measured in any stars to date, which they interpret as the odd-even fingerprint of nucleosynthesis in Pop III stars. We note, as seen in Fig. 3.4, that these three stars are all centrally located (<1 R_h).

Subsequently, Vargas et al. (2013) reported a higher metallicity spread ($-3.4 <$

[Fe/H] < -2) and a spread in α-elements ($-0.9 <$ [α/Fe] < 0) from 10 more stars from med-res spectroscopy. They conclude that the low [α/Fe] ratios at the highest [Fe/H] are caused by iron contributions from SNIa. This is difficult to reconcile with the "one-shot" model above.

In this analysis, we present HRS of two new stars on the outskirts of Com Ber ($\sim$2.5 R_h). These two stars span the same metallicity range as the three previously studied inner stars by Frebel et al. (2010a), i.e., $-3 <$ [Fe/H] < -2. This strongly suggests that they formed at the same time as the inner stars, perhaps arriving at their current locations either through tidal stripping with the MW halo or bursty feedback during star formation (i.e., Chiti et al., 2021). To examine these options further, we evaluate the detailed chemical abundances from HRS studies of the Com Ber stars. Our work is presented as both LTE and NLTE abundances in Figs. 3.5 and 3.6 for ease of comparison with the previous LTE analysis. We notice three particular chemical signatures;

- All five Com Ber stars follow a tightly decreasing [Mg/Fe] and [Ca/Fe] (and possibly [Na/Fe], acting as an α-element), with increasing [Fe/H]. The relationship is so tight that it strongly favours late iron contributions from SN Ia, as originally suggested by Vargas et al. (2013). We also note that this is in contrast to the relationships between [Mg,Ca/Fe] for the stars in Segue I and possibly Hercules.

- The [Ni/Fe] abundances also seem to decrease with [Fe/H], similar to the Ni-Na signature seen in other dwarf galaxies and MW accreted stars (Nissen & Schuster, 1997, 2010; Venn et al., 2004). Only the most metal-enhanced star CB-2 deviates from this trend, where [Ni/Fe]$\sim +0.5$. This is a very unusual signature, verified by the strength of the Ni I lines in Fig. 3.3. One possibility might be the late contributions from near-Chandrasekhar mass (M_{Ch}) white dwarfs in a double-degenerate SNIa (e.g., Kobayashi et al., 2006, 2020a; Kirby et al., 2019). As this star fits the [α/Fe] trends of the whole system quite well, then we propose it may have been moved to its location near 3 R_h due to feedback from the event(s) that also lead to its Ni-enrichment.

- The [Ba/Fe] abundances in our outermost stars are not as low as some of the previously analysed inner-most stars. Again, this is difficult to reconcile with the "one-shot" chemical evolution model for Com Ber. This is in contrast to

[Ba/Fe] in Segue I, and in better agreement with the majority of stars analysed in Hercules.

Given the detailed chemical signatures for 3 inner and 2 outer stars in Com Ber, we favour a scenario where these stars formed together in the inner regions with sufficient time for SN Ia contributions. This explains the position in [Fe/H] of the [α/Fe] knee, known to be at lower metallicities in dwarf galaxies with slower star formation histories (Tolstoy et al., 2009; Hasselquist et al., 2021). This also suggests that the outermost stars were relocated to their current outer positions *after* contributions in the central regions from SN Ia. The unusually low [Ba/H] ratios for two of the innermost stars remains a puzzle. If the barium is primarily generated through r-process, then the low barium signature may be due to a low-yield but robust r-process source (Ji et al., 2019). Another option may be due to inhomogeneous mixing of contributions from metal-poor AGB stars. If the rise in [Ba/H] (seen in Fig. 3.6) is from slow-neutron captures in AGB stars, whose yields depend on both stellar mass and metallicity (Herwig, 2005; Nomoto et al., 2013), then a wide range in [Ba/H] is possible. Combining the similar timescales for AGB and SNIa contributions, this implies that the mixing timescales of these products into star forming gas could have been very stochastic to result in low [Ba/H] at higher [Fe/H] values. The Ni enrichment in our outermost and Fe-enriched star supports this suggestion further, as contributions from sub-Ch mass white dwarfs would also require additional time. Thus, we suggest an alternative explanation to the "one shot" model for the low [Ba/Fe] ratios seen at higher [Fe/H] values for two inner stars, i.e., stochastically sampled yields from metal-poor AGB stars and SNIa in an inefficient star forming environment (i.e., an UFD). Again, we suggest the outermost stars moved to their current locations *after* these phases of chemical evolution.

3.7.2.b Boötes I

Boo I is a UFD with total mass $M \approx 1.1 \times 10^7 M_\odot$ (Muñoz et al., 2006), half-light radius $R_h \approx 217$ pc, and is fairly close to the MW at a distance of $D \approx 66$ kpc (McConnachie, 2012). Boo I is one of the brightest UFDs, with $L \approx 10^5 L_\odot$ (Muñoz et al., 2006), with apparent and absolute magnitudes of $m_V \approx 12.8$ and $M_V \approx$ -6.3 (McConnachie, 2012). Because of this, Boo I is one of the most observed UFDs with nearly 70 confirmed members, and high-resolution spectroscopic chemical abundances for 18 stars (Feltzing et al., 2009; Norris et al., 2010b; Gilmore et al., 2013; Ishigaki

et al., 2014; Frebel et al., 2016); this can also be seen in Fig. 3.1.

Photometric studies have found that Boo I has a narrow CMD at the MSTO, indicating an old single-age population (13.7 Gyr; Okamoto et al., 2012). However, HST photometry suggests there may be two ancient populations with a very small age spread (Brown et al., 2014). A kinematic study by Koposov et al. (2011) found two distinct (hot and cold) components with different velocity dispersions and mean metallicities. Furthermore, Belokurov et al. (2006) and Okamoto et al. (2012) noted an irregular morphology which may be related to tidal disruption. This was confirmed and studied further with confirmed outer members by Longeard et al. (2022).

To this discussion, we add HRS for one new outer star, at $\sim 4R_h$. This is one of the most distant stars in Boo I, and notably it is on the opposite side from the other two outermost stars with HRS. Its radial velocity and low metallicity are consistent with the inner region stars. Overall, the three outer stars with HRS have a metallicity distribution similar to the inner stars, although some stars in the central regions are slightly metal-enhanced (see Fig. 3.4). The metal-enhanced inner stars may suggest that a small amount of ongoing star formation and chemical enrichment occurred at later times. An interesting alternative to this simple scenario is the possibility that the outer stars represent a metal-poor stellar halo, e.g., from the collapse of an inhomogeneous system of star forming clouds, or even a dwarf galaxy minor merger (e.g., Benítez-Llambay et al., 2016; Deason et al., 2022).

To explore this further, we examine the detailed chemical abundances of the stars associated with Boo I. Norris et al. (2010b), Lai et al. (2011), and Gilmore et al. (2013) showed that the stars in Boo I have a wide range in metallicity ($-3.8 <$ [Fe/H] < -1.8) and a large spread in [C/Fe] (although Ishigaki et al. 2014 showed this is restricted to the very metal-poor stars with [Fe/H] < -2.7). Gilmore et al. (2013) suggested two discrete paths for chemical enrichment at low metallicity in Boo I; one where CEMP-no (carbon-enhanced metal poor stars that show no enrichment in s- or r-process; [C/Fe] > 0.7, e.g., Aoki et al. 2013) stars form rapidly and early, and a second path that forms carbon-normal stars ([C/Fe] < 0.7). They suggested these two paths may be from different dwarf galaxy progenitors which merged, or may be due to inhomogenous mixing of the SN ejecta in the ISM during subsequent star formation events.

Looking into these two scenarios, we note that the outer stars studied by Lai et al. (2011) are all carbon-normal, and the three outer stars with HRS in Boo I are also carbon-normal. In fact, their full chemical analyses suggest they are similar to

one another (in [X/Fe]), as well as to other very metal-poor stars in the MW halo. This includes our star (BooI-2) as shown in Figs. 3.5 and 3.6 (with the exception of Na), and we do not see any evidence for carbon enhancements, e.g., no strong C_2 Swan bands near 5200Å nor CH/CN features near 4300 Å. Similarly, the most metal-poor star associated with Boo I (Boo-1137; Norris et al. 2010b) has normal MW halo-like abundances extending from C through Zn, including the heavy elements Sr and Ba. Finding that all of the outer stars analysed spectroscopy are carbon-normal is not necessarily inconsistent with the low percentage of CEMP stars in Boo I. Lai et al. (2011) suggested that only 12% of the Boo I stars are CEMP, thus finding four outer stars that are metal-poor and C-normal is statistically consistent with being drawn from the inner sample, e.g., through tidal stripping. Alternatively, as they also appear to be chemically consistent with one another, formation in a separate dwarf galaxy that merged later is also plausible (e.g., Benítez-Llambay et al., 2016; Deason et al., 2022). A HRS analysis of more metal-poor stars in the outskirts of Boo I could provide indicators of formation in a previously independent and lower mass dwarf galaxy (e.g., a lower [α/Fe] knee). This could help to address whether this UFD underwent a minor merger that provided stars that now occupy a halo.

As a final comment, two additional chemical evolution models for Boo I suggest that very inefficient star formation turned less than 3% of the baryons into stars (Vincenzo et al., 2014) and that bursty star formation episodes and supernova events were not the dominant sources of the gas removal (Romano et al., 2015). The latter also suggested that external mechanisms are needed to model this UFD (e.g., the absence of neutral gas, Bailin & Ford 2007), in addition to the outermost stars.

3.7.2.c UMa I

UMa I is a UFD with total mass $M \approx 1.5 \times 10^7 M_\odot$ (Simon & Geha, 2007), apparent and absolute magnitudes of $m_V \approx 14.4$ and $M_V \approx$ -5.5, half-light radius $R_h \approx 235$ pc, and it is at a distance of $D \approx 97$ kpc (McConnachie, 2012). HST photometry showed that UMa I has an age within 1 Gyr of the oldest known MW globular cluster, M92 (Brown et al., 2012). Furthermore, Brown et al. (2014) reconstructed its star formation history with a two-burst model, such that roughly half of the stars in UMa I were formed over 13 Gyr ago, and the other half by $z \sim 3$ (11.6 Gyr ago). They also suggest that a physical distortion in the structure of UMa I may account for the apparent age spread, e.g., a tidal distortion, first noticed in a photometric study by

Okamoto et al. (2008), A dynamical analysis using radial velocities and Gaia DR2 proper motion data found that UMa I is within 4 kpc of pericenter (Simon, 2018; Fritz et al., 2018), and may even be a "backsplash" satellite, in that its orbit may have taken it beyond the virial radius of the MW dark matter halo. For a galaxy at this distance, no more than 15-20% of its stars are thought to be vulnerable to tidal stripping (Simon, 2019). However, the elongated shape of UMa I is distinct and upon first glance many suspect this is a result of tidal interactions. As seen in Borukhovetskaya et al. (2022), pericenter estimates can be very sensitive to measured distances and proper motions, therefore decisions based on the locations of the outer stars in UMa I as a result of tidal stripping should be reserved until precise orbits have been determined.

UMa I is slightly further than Com Ber or Boo I, so previous studies have been restricted to MRS analyses, or radial velocities only from HRS (Kleyna et al., 2005; Simon & Geha, 2007; Martin et al., 2007; Vargas et al., 2013). Here, we provide the first HRS model atmospheres analyses of two stars in UMa I. Radial velocities are in good agreement with MRS estimates in the literature. Our two UMa I targets include one inner star ($< 1R_h$) and one in the outskirts ($\sim 4R_h$); see Fig. 3.4. The two stars have similar metallicities and chemical abundances, suggesting that they formed from the same or similar interstellar gas.

Some of the inner stars in UMa I may be more metal-rich than the two in this analysis (see Fig. 3.4), indicative of on-going or bursty star formation with inhomogeneous mixing of the gas in the central regions. The position of our outermost star could then be explained by bursty feedback associated with this star formation epoch. The very low [Na/Fe] abundances we find in our two UMa I stars also favour a later formation time, if the low values observed are due to later contributions to Fe-only from SN Ia (as discussed above for Com Ber). More members of UMa I with a wider range in metallicity will need to be analysed to comment further on the evolutionary history of UMa I.

3.7.3 No PISN, No NSM

If the UFDs are dominated by old stellar populations, i.e., fossil relics from before reionization, then simulations predict that the stars we observe today (z=0) may include traces of the chemical signatures of very massive Population III stars (Tumlinson, 2010; Frebel & Bromm, 2012; Hartwig et al., 2018; Ishigaki et al., 2018).

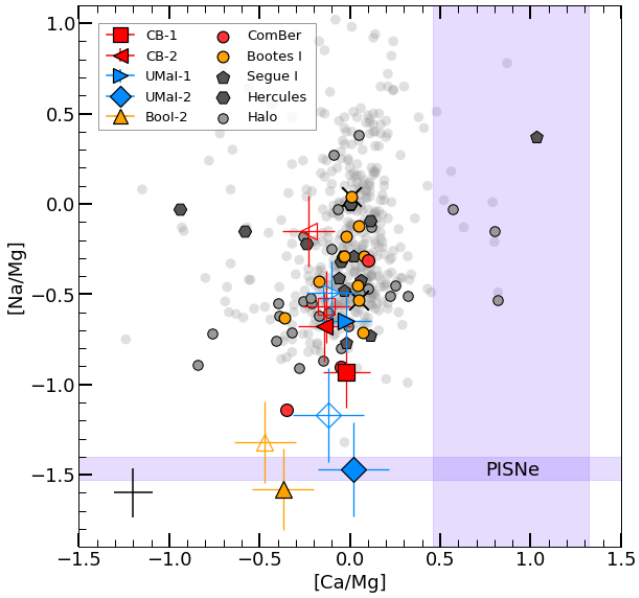

Figure 3.7: The [Ca/Mg] ratios as a function of [Na/Mg]. The shaded regions correspond to predicted PISNe yields (Takahashi et al., 2018). Two stars, UMa1-2 and BooI-2, have [Na/Mg] ratios consistent with PISNe predictions, but their [Ca/Mg] ratios are significantly lower than predictions. Thus, none of our stars nor Boo I stars from the literature match the PISNe signatures.

Pair-instability supernova (PISN) are a common fate for such massive stars. Predictions for nucleosynthesis that can take place during a PISN show unique patterns, e.g., high ratios in the certain light elements (e.g,. [Ca/Mg]), and the absence of heavy elements (e.g., [Ba/Fe]), Takahashi et al. 2018), along with the classic odd-even effect seen in the [Na/Mg] or [Al/Mg] ratios (Heger & Woosley, 2010; Salvadori et al., 2019). When the star formation history has been as slow and inefficient as in UFDs, it is reasonable to look for these chemical signatures since we expect very little later star formation to have affected the chemical evolution of the system. In Fig. 3.7, the high [Ca/Mg] ratios predicted by Takahashi et al. (2018) are compared to the very low and narrow [Na/Mg] predictions. We do not find any stars with both high [Ca/Mg] and low [Na/Mg], suggesting that the abundance patterns in these UFDs are not dominated by the ejecta from PISN.

We also mention that contributions from compact binary mergers are predicted to produce very high abundances of neutron capture elements (e.g., Korobkin et al., 2012; Wu et al., 2016), as seen in the UFD galaxy Ret II (Roederer et al., 2016; Ji et al., 2016; Ji & Frebel, 2018). No stars in these three UFD galaxies appear to have high [Ba/Fe] ratios; thus, we find no evidence for such signature of compact binary

mergers in these systems.

3.8 Conclusions

Ultra-faint dwarf galaxies are unique objects for studying galaxy formation and the early universe. This is because their old stellar populations and nearby locations in the MW halo mean that analyses of individual metal-poor stars may provide clues to physical conditions in the early Universe. In this paper, we present high-resolution spectra taken with the Gemini/GRACES spectrograph of five stars associated with the Coma Berenices, Boötes I, and Ursa Major I ultra faint dwarf galaxies. Most of these stars are in the outskirts, $> 2R_h$, but include one inner star in UMa I. Their radial velocities and metallicities are consistent with membership in these UFDs, showing that the Bayesian inference method using Gaia photometric and astrometric data (McConnachie & Venn, 2020b) is highly successful at selecting members, even at large radial distances.

The detailed model atmospheres analyses of these spectra have provided additional information on the evolution of these UFDs.

- The [α/Fe] abundances in Com Ber suggest this UFD has been enriched in iron from SN Ia. This is at odds with the previous suggestion that Com Ber is a fossil relic enriched by only one early core-collapse SN (i.e., the "one-shot" model). A star formation model that includes contributions from SN Ia is supported by an elevated Ni in the least metal-poor star, possibly due to enrichment from near-M_{Ch} mass white dwarfs. The [Ba/H] ratios vary from star to star in Com Ber, which may be more consistent with inhomogeneous mixing of AGB yields in the gas during star formation. Finally, these conclusions include the outermost stars, which suggests those stars moved to their outer locations after formation in the central regions.

- In Boötes I, the analysis of our star and two others with HRS at $> 3R_h$ show they are metal-poor and C-normal. Some inner stars may be slightly more metal-rich implying longer-lived star formation in the centre; alternatively, several newly discovered very metal-poor stars in the outerskirts suggests the halo remnant of a dwarf galaxy minor merger.

- We present the first model atmospheres abundance analysis of two stars associated with UMa I; one inner star (<1 R_h) and one in its outskirts ($R \sim 4R_h$).

The outermost star is aligned with the distorted shape of UMa I seen in its photometry. Their metallicities and chemical signatures are similar to one another, as well as the stars in other UFDs. Very low [Na/Fe] values are seen, similar to the stars in Com Ber, which may indicate a star formation history that permits contributions from SN Ia events. This suggests the outermost star moved to its current locations after its formation with the inner star in the central regions.

While single star observations are time consuming and expensive for major observatories, spectroscopic observations of carefully selected stars in the outskirts of the UFD galaxies are necessary to address questions related to the formation of the MW, dwarf-dwarf galaxy mergers, the search for the first stars, the chemical yields from metal-poor supernovae, and the chemical evolution of these unique systems.

Chapter 4

Conclusions

I present work carried out towards the successful commissioning and operation of the new Gemini High Resolution Optical SpecTrograph (GHOST) at the Gemini South Observatory, detailed in Chapter 2. I contributed towards 17 nights of commissioning between June and September 2022 doing instrument operation, record-keeping, and target selection amongst other tasks. I was one of the first to process on-sky data using the data reduction pipeline, GHOSTDR. I bug-tested GHOSTDR and developed tools to streamline the bug-testing and data processing methods, working towards the completion and refinement of the data reduction pipeline. With this experience and related expertise, I worked with the science team towards the goal of publishing our first science results. My interest in the GHOST spectrograph lay in one of its key science drivers, obtaining high-resolution spectra of UFD stars which may provide clues to physical conditions in the early universe, as I had previously conducted detailed chemical analyses of UFD stars towards this end (Waller et al., 2023).

In Chapter 3, I present the first model atmospheres abundance analysis of five stars newly associated with the Coma Berenices, Boötes I, and Ursa Major I UFD galaxies using spectra taken with the Gemini/GRACES spectrograph. Most are in the outskirts of their respective galaxies ($> 2R_h$), and were identified as likely member stars from a Bayesian inference method using Gaia photometric and astrometric data (McConnachie & Venn, 2020b; Jensen et al., 2024). Analyses of stars in outskirts may find clues to structure formation and chemical evolution, and create for a more complete census of UFD stars, of which stars bright enough to obtain HR spectra are already limited in number. Their radial velocities and metallicities found in this analysis are consistent with membership in these UFDs, showing that the Bayesian inference method is highly successful at selecting members, even at large radial distances.

The detailed model atmospheres analyses of these spectra have provided additional information on the evolution of these UFDs. Two analysis methods were performed, making use of spectra with a S/N lower than typically desired for such work, extracting as much chemical abundance information as possible while conserving expensive telescope resources.

The [α/Fe] abundances in Com Ber suggest this UFD has been enriched in iron from SN Ia. A star formation model that includes contributions from SN Ia is supported by an elevated Ni in the least metal-poor star, possibly due to enrichment from near-$M_{\rm Ch}$ mass white dwarfs. The [Ba/H] ratios vary from star to star in Com Ber, which may be more consistent with inhomogeneous mixing of AGB yields in the gas during star formation. Finally, these conclusions include the outermost stars, which suggests those stars moved to their outer locations after formation in the central regions.

In Boötes I, the analysis of our star and two others with HRS at $> 3{\rm R_h}$ show they are metal-poor and C-normal. Some inner stars may be slightly more metal-rich implying longer-lived star formation in the centre; alternatively, several newly discovered very metal-poor stars in the outskirts suggests the halo remnant of a dwarf galaxy minor merger.

UMa I had no stars with previous model atmospheres abundance analyses until the two presented here; one inner star ($<$1 R$_{\rm h}$) and one in its outskirts ($R \sim 4{\rm R_h}$). The outermost star is aligned with the distorted shape of UMa I seen in its photometry. Their metallicities and chemical signatures are similar to one another, as well as the stars in other UFDs, evidence of membership to UMa I. Very low [Na/Fe] values are seen, similar to the stars in Com Ber, which may indicate a star formation history that permits contributions from SN Ia events. This suggests the outermost star moved to its current location after its formation with the inner star in the central regions.

Spectroscopic observations of carefully selected stars in the outskirts of the UFD galaxies are necessary to address questions related to the formation of the MW, dwarf-dwarf galaxy mergers, the chemical yields from metal-poor supernovae, and the chemical evolution of these unique systems. The dual acquisition mode and exemplary sensitivity in the blue range make GHOST a powerful tool for further observations, in particular measurements of more neutron-capture elements. My contributions to commissioning and the data reduction pipeline earned co-authorship on the first science results from GHOST, obtained using commissioning data, presented in Hayes et al. (2023), Sestito et al. (2024), and Dovgal et al. (2024).

Bibliography

Abazajian K. N., et al., 2009, ApJS, 182, 543

Abbott T. M. C., et al., 2018, ApJS, 239, 18

Agertz O., et al., 2020, MNRAS, 491, 1656

Akins H. B., Christensen C. R., Brooks A. M., Munshi F., Applebaum E., Engelhardt A., Chamberland L., 2021, ApJ, 909, 139

Andrae R., et al., 2018, A&A, 616, A8

Andrievsky S. M., Spite M., Korotin S. A., Spite F., Bonifacio P., Cayrel R., François P., Hill V., 2010, A&A, 509, A88

Aoki W., et al., 2013, AJ, 145, 13

Applebaum E., Brooks A. M., Christensen C. R., Munshi F., Quinn T. R., Shen S., Tremmel M., 2021, ApJ, 906, 96

Arlandini C., Käppeler F., Wisshak K., Gallino R., Lugaro M., Busso M., Straniero O., 1999, ApJ, 525, 886

Asplund M., Grevesse N., Sauval A. J., Scott P., 2009, ARA&A, 47, 481

Bailin J., Ford A., 2007, MNRAS, 375, L41

Bastian N., Lardo C., 2018, ARA&A, 56, 83

Battaglia G., Taibi S., Thomas G. F., Fritz T. K., 2022, A&A, 657, A54

Battistini C., Bensby T., 2015, A&A, 577, A9

Baumgardt H., Hilker M., 2018, MNRAS, 478, 1520

Bechtol K., et al., 2015, ApJ, 807, 50

Belokurov V., et al., 2006, ApJ, 647, L111

Belokurov V., Erkal D., Evans N. W., Koposov S. E., Deason A. J., 2018, MNRAS, 478, 611

Benítez-Llambay A., Navarro J. F., Abadi M. G., Gottlöber S., Yepes G., Hoffman Y., Steinmetz M., 2016, MNRAS, 456, 1185

Bergemann M., 2011, MNRAS, 413, 2184

Bergemann M., Cescutti G., 2010, A&A, 522, A9

Bergemann M., Lind K., Collet R., Magic Z., Asplund M., 2012, MNRAS, 427, 27

Bergemann M., Collet R., Amarsi A. M., Kovalev M., Ruchti G., Magic Z., 2017, ApJ, 847, 15

Bernstein R., Shectman S. A., Gunnels S. M., Mochnacki S., Athey A. E., 2003, in Iye M., Moorwood A. F. M., eds, Society of Photo-Optical Instrumentation Engineers (SPIE) Conference Series Vol. 4841, Instrument Design and Performance for Optical/Infrared Ground-based Telescopes. pp 1694–1704, doi:10.1117/12.461502

Bisterzo S., Travaglio C., Gallino R., Wiescher M., Käppeler F., 2014, ApJ, 787, 10

Borukhovetskaya A., Errani R., Navarro J. F., Fattahi A., Santos-Santos I., 2022, MNRAS, 509, 5330

Bressan A., Marigo P., Girardi L., Salasnich B., Dal Cero C., Rubele S., Nanni A., 2012, MNRAS, 427, 127

Brown T. M., et al., 2012, ApJ, 753, L21

Brown T. M., et al., 2014, ApJ, 796, 91

Bullock J. S., Boylan-Kolchin M., 2017a, ARA&A, 55, 343

Bullock J. S., Boylan-Kolchin M., 2017b, ARA&A, 55, 343

Bullock J. S., Johnston K. V., 2005, ApJ, 635, 931

Burgers A., 2015

Busso M., Gallino R., Wasserburg G. J., 1999, ARA&A, 37, 239

Carretta E., et al., 2009, Astronomy & Astrophysics, 505, 117

Casagrande L., 2020, in IAU General Assembly. pp 465–465, doi:10.1017/S1743921319005118

Chambers K. C., et al., 2016, arXiv e-prints, p. arXiv:1612.05560

Chene A.-N., et al., 2014, in Navarro R., Cunningham C. R., Barto A. A., eds, Society of Photo-Optical Instrumentation Engineers (SPIE) Conference Series Vol. 9151, Advances in Optical and Mechanical Technologies for Telescopes and Instrumentation. p. 915147 (arXiv:1409.7448), doi:10.1117/12.2057417

Chiti A., et al., 2021, Nature Astronomy, 5, 392

Choi J., Dotter A., Conroy C., Cantiello M., Paxton B., Johnson B. D., 2016, ApJ, 823, 102

Churilov V., et al., 2018, in Evans C. J., Simard L., Takami H., eds, Vol. 10702, Ground-based and Airborne Instrumentation for Astronomy VII. SPIE, pp 1887 – 1898, doi:10.1117/12.2312401, https://doi.org/10.1117/12.2312401

Cropper M., et al., 2018, A&A, 616, A5

Curtis-Lake E., et al., 2023, Nature Astronomy, 7, 622

Deason A. J., Bose S., Fattahi A., Amorisco N. C., Hellwing W., Frenk C. S., 2022, MNRAS, 511, 4044

Dekker H., D'Odorico S., Kaufer A., Delabre B., Kotzlowski H., 2000, in Iye M., Moorwood A. F., eds, Society of Photo-Optical Instrumentation Engineers (SPIE) Conference Series Vol. 4008, Optical and IR Telescope Instrumentation and Detectors. pp 534–545, doi:10.1117/12.395512

Demarque P., Woo J.-H., Kim Y.-C., Yi S. K., 2004, ApJS, 155, 667

Dotter A., 2016, ApJS, 222, 8

Dovgal A., et al., 2024, MNRAS, 527, 7810

El-Badry K., et al., 2018, MNRAS, 476, 528

Farrell T., Robertson G., Neilson J., Burley G., Margheim S., McDermid R., Young P., 2022, Gemini High-Resolution Optical Spectrograph (GHOST) Users Manual. Australia National University, NRC-Herzberg, Australian Astronomical Optics Macquarie, Gemini Observatory

Feltzing S., Eriksson K., Kleyna J., Wilkinson M. I., 2009, A&A, 508, L1

Fenner Y., Gibson B. K., Gallino R., Lugaro M., 2006, ApJ, 646, 184

François P., Monaco L., Bonifacio P., Moni Bidin C., Geisler D., Sbordone L., 2016, A&A, 588, A7

Frebel A., Bromm V., 2012, ApJ, 759, 115

Frebel A., Simon J. D., Geha M., Willman B., 2010a, ApJ, 708, 560

Frebel A., Simon J. D., Geha M., Willman B., 2010b, ApJ, 708, 560

Frebel A., Simon J. D., Kirby E. N., 2014, ApJ, 786, 74

Frebel A., Norris J. E., Gilmore G., Wyse R. F. G., 2016, ApJ, 826, 110

Frenk C. S., White S. D. M., Davis M., Efstathiou G., 1988, ApJ, 327, 507

Fritz T. K., Battaglia G., Pawlowski M. S., Kallivayalil N., van der Marel R., Sohn S. T., Brook C., Besla G., 2018, A&A, 619, A103

Gaia Collaboration et al., 2016a, A&A, 595, A1

Gaia Collaboration et al., 2016b, A&A, 595, A1

Gaia Collaboration et al., 2018a, A&A, 616, A1

Gaia Collaboration et al., 2018b, A&A, 616, A11

Gaia Collaboration et al., 2021, A&A, 649, A1

Gilmore G., et al., 2013, The Messenger, 151, 25

González Hernández J. I., Bonifacio P., 2009, A&A, 497, 497

Gustafsson B., Edvardsson B., Eriksson K., Jørgensen U. G., Nordlund Å., Plez B., 2008, A&A, 486, 951

Hansen T. T., et al., 2017, ApJ, 838, 44

Hartwig T., et al., 2018, MNRAS, 478, 1795

Hasselquist S., et al., 2021, ApJ, 923, 172

Hayes C. R., et al., 2022, in Evans C. J., Bryant J. J., Motohara K., eds, Vol. 12184, Ground-based and Airborne Instrumentation for Astronomy IX. SPIE, p. 121846H, doi:10.1117/12.2642905, https://doi.org/10.1117/12.2642905

Hayes C. R., et al., 2023, ApJ, 955, 17

Heger A., Woosley S. E., 2010, ApJ, 724, 341

Heintz K. E., et al., 2023, Nature Astronomy, 7, 1517

Helmi A., 2020, ARA&A, 58, 205

Helmi A., Babusiaux C., Koppelman H. H., Massari D., Veljanoski J., Brown A. G. A., 2018, Nature, 563, 85

Herwig F., 2005, ARA&A, 43, 435

Ibata R., Irwin M., Lewis G. F., Stolte A., 2001, ApJ, 547, L133

Ibata R., et al., 2021, ApJ, 914, 123

Imig J., et al., 2023, ApJ, 954, 124

Ireland M., et al., 2014, in Ramsay S. K., McLean I. S., Takami H., eds, Society of Photo-Optical Instrumentation Engineers (SPIE) Conference Series Vol. 9147, Ground-based and Airborne Instrumentation for Astronomy V. p. 91471J, doi:10.1117/12.2057356

Ireland M. J., et al., 2016, in Evans C. J., Simard L., Takami H., eds, Society of Photo-Optical Instrumentation Engineers (SPIE) Conference Series Vol. 9908, Ground-based and Airborne Instrumentation for Astronomy VI. p. 99087A, doi:10.1117/12.2233927

Ireland M. J., White M., Bento J. P., Farrell T., Labrie K., Luvaul L., Nielsen J. G., Simpson C., 2018, in Guzman J. C., Ibsen J., eds, Society of Photo-Optical Instrumentation Engineers (SPIE) Conference Series Vol. 10707, Software and Cyberinfrastructure for Astronomy V. p. 1070735, doi:10.1117/12.2314418

Ishigaki M. N., Tominaga N., Kobayashi C., Nomoto K., 2014, ApJ, 792, L32

Ishigaki M. N., Tominaga N., Kobayashi C., Nomoto K., 2018, ApJ, 857, 46

Jenkins S. A., Li T. S., Pace A. B., Ji A. P., Koposov S. E., Mutlu-Pakdil B., 2021, ApJ, 920, 92

Jensen J., Hayes C. R., Sestito F., McConnachie A. W., Waller F., Smith S. E. T., Navarro J., Venn K. A., 2024, MNRAS, 527, 4209

Ji A. P., Frebel A., 2018, ApJ, 856, 138

Ji A. P., Frebel A., Chiti A., Simon J. D., 2016, Nature, 531, 610

Ji A. P., Simon J. D., Frebel A., Venn K. A., Hansen T. T., 2019, ApJ, 870, 83

Ji A. P., et al., 2023, AJ, 165, 100

Karovicova I., White T. R., Nordlander T., Casagrande L., Ireland M., Huber D., Jofré P., 2020, A&A, 640, A25

Kielty C. L., et al., 2021, MNRAS, 506, 1438

Kirby E. N., et al., 2019, ApJ, 881, 45

Kleyna J. T., Wilkinson M. I., Evans N. W., Gilmore G., 2005, ApJ, 630, L141

Kobayashi C., Nomoto K., 2009, ApJ, 707, 1466

Kobayashi C., Umeda H., Nomoto K., Tominaga N., Ohkubo T., 2006, ApJ, 653, 1145

Kobayashi C., Leung S.-C., Nomoto K., 2020a, ApJ, 895, 138

Kobayashi C., Karakas A. I., Lugaro M., 2020b, ApJ, 900, 179

Koch A., McWilliam A., Grebel E. K., Zucker D. B., Belokurov V., 2008, ApJ, 688, L13

Koch A., Feltzing S., Adén D., Matteucci F., 2013, A&A, 554, A5

Koposov S. E., et al., 2011, ApJ, 736, 146

Korobkin O., Rosswog S., Arcones A., Winteler C., 2012, MNRAS, 426, 1940

Kraft R. P., Ivans I. I., 2003, PASP, 115, 143

Labrie K., Anderson K., Cárdenes R., Simpson C., Turner J. E. H., 2019, in Teuben P. J., Pound M. W., Thomas B. A., Warner E. M., eds, Astronomical Society of the Pacific Conference Series Vol. 523, Astronomical Data Analysis Software and Systems XXVII. p. 321

Laevens B. P. M., et al., 2015, ApJ, 802, L18

Lai D. K., Lee Y. S., Bolte M., Lucatello S., Beers T. C., Johnson J. A., Sivarani T., Rockosi C. M., 2011, ApJ, 738, 51

Leaman R., 2012, AJ, 144, 183

Lejeune T., Cuisinier F., Buser R., 1998, A&AS, 130, 65

Li T. S., et al., 2022, ApJ, 928, 30

Limongi M., Chieffi A., 2018, ApJS, 237, 13

Lind K., Bergemann M., Asplund M., 2012, MNRAS, 427, 50

Lindegren L., et al., 2021, A&A, 649, A2

Longeard N., et al., 2022, MNRAS,

Malhan K., Ibata R. A., Carlberg R. G., Bellazzini M., Famaey B., Martin N. F., 2019, ApJ, 886, L7

Martin N. F., Ibata R. A., Chapman S. C., Irwin M., Lewis G. F., 2007, MNRAS, 380, 281

Martin N. F., et al., 2022a, arXiv e-prints, p. arXiv:2201.01310

Martin N. F., et al., 2022b, Nature, 601, 45

Martioli E., Teeple D., Manset N., Devost D., Withington K., Venne A., Tannock M., 2012, Open source pipeline for ESPaDOnS reduction and analysis. SPIE, p. 84512B, doi:10.1117/12.926627

Mashonkina L. I., Belyaev A. K., 2019, Astronomy Letters, 45, 341

Mashonkina L., Jablonka P., Pakhomov Y., Sitnova T., North P., 2017, A&A, 604, A129

McConnachie A. W., 2012, AJ, 144, 4

McConnachie A. W., Venn K. A., 2020a, AJ, 160, 124

McConnachie A. W., Venn K. A., 2020b, AJ, 160, 124

McConnachie A. W., Hayes C. R., Pazder J., Ireland M. J., Kalari V. M., McDermid R. M., Margheim S., 2022a, Nature Astronomy, 6, 1491

McConnachie A. W., et al., 2022b, in Evans C. J., Bryant J. J., Motohara K., eds, Society of Photo-Optical Instrumentation Engineers (SPIE) Conference Series Vol. 12184, Ground-based and Airborne Instrumentation for Astronomy IX. p. 121841E, doi:10.1117/12.2630407

McConnachie A. W., et al., 2024, arXiv e-prints, p. arXiv:2401.07452

McNish L., 2018, Solar Spectrum, https://calgary.rasc.ca/solarspectrum.htm

Muñoz R. R., Carlin J. L., Frinchaboy P. M., Nidever D. L., Majewski S. R., Patterson R. J., 2006, ApJ, 650, L51

Mucciarelli A., Bellazzini M., 2020, Research Notes of the American Astronomical Society, 4, 52

Munroe R., 2016, Solar Spectrum, https://xkcd.com/1733/

NOIRLab International Gemini Observatory NSF AURA GHOST Consortium 2022, Gemini's GHOST Captures Exquisite First Light Observations of a Bright, Chemically Rich Star, https://noirlab.edu/public/news/noirlab2217/

Nissen P. E., Schuster W. J., 1997, A&A, 326, 751

Nissen P. E., Schuster W. J., 2010, A&A, 511, L10

Nomoto K., Kobayashi C., Tominaga N., 2013, ARA&A, 51, 457

Norris J. E., Yong D., Gilmore G., Wyse R. F. G., 2010a, ApJ, 711, 350

Norris J. E., Wyse R. F. G., Gilmore G., Yong D., Frebel A., Wilkinson M. I., Belokurov V., Zucker D. B., 2010b, ApJ, 723, 1632

Oesch P. A., et al., 2014, ApJ, 786, 108

Okamoto S., Arimoto N., Yamada Y., Onodera M., 2008, A&A, 487, 103

Okamoto S., Arimoto N., Yamada Y., Onodera M., 2012, ApJ, 744, 96

Pace A. B., Li T. S., 2019, ApJ, 875, 77

Pace A. B., Erkal D., Li T. S., 2022, ApJ, 940, 136

Paxton B., Bildsten L., Dotter A., Herwig F., Lesaffre P., Timmes F., 2011, ApJS, 192, 3

Pazder J., Fournier P., Pawluczyk R., van Kooten M., 2014, in Navarro R., Cunningham C. R., Barto A. A., eds, Society of Photo-Optical Instrumentation Engineers (SPIE) Conference Series Vol. 9151, Advances in Optical and Mechanical Technologies for Telescopes and Instrumentation. p. 915124, doi:10.1117/12.2057327

Pazder J., Burley G., Ireland M. J., Robertson G., Sheinis A., Zhelem R., 2016, in Evans C. J., Simard L., Takami H., eds, Vol. 9908, Ground-based and Airborne Instrumentation for Astronomy VI. SPIE, pp 2195 – 2205, doi:10.1117/12.2234366, https://doi.org/10.1117/12.2234366

Pazder J., et al., 2020, in Society of Photo-Optical Instrumentation Engineers (SPIE) Conference Series. p. 1144743, doi:10.1117/12.2561985

Pazder J., Anthony A., McConnachie A., Burley G., 2022, in Evans C. J., Bryant J. J., Motohara K., eds, Society of Photo-Optical Instrumentation Engineers (SPIE) Conference Series Vol. 12184, Ground-based and Airborne Instrumentation for Astronomy IX. p. 1218453, doi:10.1117/12.2630620

Placco V. M., Sneden C., Roederer I. U., Lawler J. E., Den Hartog E. A., Hejazi N., Maas Z., Bernath P., 2021, Research Notes of the American Astronomical Society, 5, 92

Reggiani H., Meléndez J., Kobayashi C., Karakas A., Placco V., 2017, A&A, 608, A46

Revaz Y., Jablonka P., 2018, A&A, 616, A96

Rey M. P., Pontzen A., Agertz O., Orkney M. D. A., Read J. I., Rosdahl J., 2020, MNRAS, 497, 1508

Ricotti M., Gnedin N. Y., Shull J. M., 2008, ApJ, 685, 21

Riello M., et al., 2021, A&A, 649, A3

Roederer I. U., Preston G. W., Thompson I. B., Shectman S. A., Sneden C., Burley G. S., Kelson D. D., 2014, AJ, 147, 136

Roederer I. U., Karakas A. I., Pignatari M., Herwig F., 2016, ApJ, 821, 37

Roederer I. U., et al., 2022, ApJS, 260, 27

Roederer I. U., Pace A. B., Placco V. M., Caldwell N., Koposov S. E., Mateo M., Olszewski E. W., Walker M. G., 2023, ApJ, 954, 55

Romano D., Bellazzini M., Starkenburg E., Leaman R., 2015, MNRAS, 446, 4220

Salvadori S., Bonifacio P., Caffau E., Korotin S., Andreevsky S., Spite M., Skúladóttir Á., 2019, MNRAS, 487, 4261

Schlegel D. J., Finkbeiner D. P., Davis M., 1998, ApJ, 500, 525

Seeger P. A., Fowler W. A., Clayton D. D., 1965, ApJS, 11, 121

Sestito F., et al., 2023, MNRAS, 525, 2875

Sestito F., et al., 2024, MNRAS,

Simon J. D., 2018, ApJ, 863, 89

Simon J. D., 2019, ARA&A, 57, 375

Simon J. D., Geha M., 2007, ApJ, 670, 313

Sitnova T. M., et al., 2021, MNRAS, 504, 1183

Skúladóttir Á., Hansen C. J., Salvadori S., Choplin A., 2019, A&A, 631, A171

Smith S. E. T., et al., 2023, AJ, 166, 76

Sneden C., 1973, ApJ, 184, 839

Sneden C., Cowan J. J., Gallino R., 2008, ARA&A, 46, 241

Sobeck J. S., et al., 2011, AJ, 141, 175

Starkenburg E., Oman K. A., Navarro J. F., Crain R. A., Fattahi A., Frenk C. S., Sawala T., Schaye J., 2017a, MNRAS, 465, 2212

Starkenburg E., et al., 2017b, MNRAS, 471, 2587

Su K.-Y., et al., 2018, MNRAS, 480, 1666

Takahashi K., Yoshida T., Umeda H., 2018, ApJ, 857, 111

Tanvir N. R., et al., 2017a, ApJ, 848, L27

Tanvir N. R., et al., 2017b, ApJ, 848, L27

Thomas G. F., Battaglia G., 2022, A&A, 660, A29

Timmes F. X., Woosley S. E., Hartmann D. H., Hoffman R. D., Weaver T. A., Matteucci F., 1995, ApJ, 449, 204

Tody D., 1986, in Crawford D. L., ed., Society of Photo-Optical Instrumentation Engineers (SPIE) Conference Series Vol. 627, Society of Photo-Optical Instrumentation Engineers (SPIE). p. 733, doi:10.1117/12.968154

Tody D., 1993, in Hanisch R. J., Brissenden R. J. V., Barnes J., eds, Astronomical Society of the Pacific Conference Series Vol. 52, Astronomical Data Analysis Software and Systems II. p. 173

Tolstoy E., Hill V., Tosi M., 2009, ARA&A, 47, 371

Tumlinson J., 2010, ApJ, 708, 1398

VandenBerg D. A., Swenson F. J., Rogers F. J., Iglesias C. A., Alexander D. R., 2000, ApJ, 532, 430

Vargas L. C., Geha M., Kirby E. N., Simon J. D., 2013, ApJ, 767, 134

Venn K. A., Irwin M., Shetrone M. D., Tout C. A., Hill V., Tolstoy E., 2004, AJ, 128, 1177

Venn K. A., Starkenburg E., Malo L., Martin N., Laevens B. P. M., 2017, MNRAS, 466, 3741

Vincenzo F., Matteucci F., Vattakunnel S., Lanfranchi G. A., 2014, MNRAS, 441, 2815

Vincenzo F., Kobayashi C., Taylor P., 2018, MNRAS, 480, L38

Vogt S. S., et al., 1994, in Crawford D. L., Craine E. R., eds, Society of Photo-Optical Instrumentation Engineers (SPIE) Conference Series Vol. 2198, Instrumentation in Astronomy VIII. p. 362, doi:10.1117/12.176725

Waller F., et al., 2023, MNRAS, 519, 1349

Wanajo S., 2013, ApJ, 770, L22

Weisz D. R., Dolphin A. E., Skillman E. D., Holtzman J., Gilbert K. M., Dalcanton J. J., Williams B. F., 2014, ApJ, 789, 147

Wetzel A. R., Deason A. J., Garrison-Kimmel S., 2015, ApJ, 807, 49

Wheeler C., Oñorbe J., Bullock J. S., Boylan-Kolchin M., Elbert O. D., Garrison-Kimmel S., Hopkins P. F., Kereš D., 2015, MNRAS, 453, 1305

Wheeler C., et al., 2019, MNRAS, 490, 4447

White S. D. M., Rees M. J., 1978, MNRAS, 183, 341

Woosley S. E., Hoffman R. D., 1992, ApJ, 395, 202

Woosley S. E., Weaver T. A., 1995, ApJS, 101, 181

Wu M.-R., Fernández R., Martínez-Pinedo G., Metzger B. D., 2016, MNRAS, 463, 2323

Yong D., et al., 2013, ApJ, 762, 26

Yong D., et al., 2021, MNRAS, 507, 4102

York D. G., et al., 2000, AJ, 120, 1579

Zhelem R., et al., 2018, in Evans C. J., Simard L., Takami H., eds, Vol. 10702, Ground-based and Airborne Instrumentation for Astronomy VII. SPIE, pp 1979 – 1994, doi:10.1117/12.2313059, https://doi.org/10.1117/12.2313059

Zhelem R., et al., 2020, in Ellis S. C., d'Orgeville C., eds, Vol. 11203, Advances in Optical Astronomical Instrumentation 2019. SPIE, pp 85 – 86, doi:10.1117/12.2539924, https://doi.org/10.1117/12.2539924

van de Ven G., van den Bosch R. C. E., Verolme E. K., de Zeeuw P. T., 2006, A&A, 445, 513